



Norwegian University of  
Science and Technology

# Morphing skins to improve local flow behavior in a hydroturbine context

Adaptive overflater for forbedring av lokal strømning i  
vannturbinsammenheng

**Jarle Vikør Ekanger**

Master of Science in Energy and Environment

Submission date: June 2011

Supervisor: Morten Kjeldsen, EPT

Co-supervisor: Håkon Hjort Francke, Flow Design Bureau AS



EPT-M-2011-28

## MASTER THESIS

for

Stud.techn. Jarle Vikør Ekanger  
Spring 2011

### *Morphing skins to improve local flow behavior in a hydroturbine context*

*Adaptive overflater for forbedring av lokal strømming i vannturbinsammenheng*

#### **Background and objective.**

Many of the operation problems in hydroturbines such as reduced performance, noise and vibration, and sand erosion are due to the presence of secondary flow fields. These flow fields are naturally present due to the existence of gaps and boundary layers (BL). Gaps create leakage flows, while BL- solid structure interaction can create swirls, and finally BL separation can create large scale instabilities. When hydroturbines are operated outside of their design range the strength of such secondary flow fields can increase dramatically. This increase can be attributed erroneous design for the given (off design) operation point. Evidently a better performance can be achieved if the turbine geometry adapts to the new operation point<sup>1</sup>.

The aerospace industries have been investigating the possibility of morphing skins, e.g. as a substitute for hinged flaps, for decades. Their motivation for morphing skins, or adaptive aerodynamic shapes, being the highly different operation points for airplanes; i.e. take-off and landing versus cruise, and supersonic versus subsonic flight.

The objective of this study is therefore to identify a number of secondary flow fields causing problematic operation. Also possible (practical) morphing skin solutions should be considered, and how they can affect the flow fields identified above. Based on the suggested solutions a control procedure should be developed.

---

<sup>1</sup> Kaplan turbine includes an adaption by changing the angle of attack of the runner blades when the load level is changed.

**The following questions should be considered in the project work:**

- 1 A literature study establishing state of the art shall be made. Special focus should be given whether solutions with the aerospace industries can be applied in water.
- 2 The use of CFD shall be applied to (as a minimum) quantitatively assess the design approach. Note simple or generic geometries such as a bend can be used for the analysis.
- 3 A focus on practical skins and actuation of the same shall be given.
- 4 An experiment shall be designed where the concept of morphing skins can be demonstrated. The experiment shall include a sensor, controller and actuator chain. Note: There is an external interest, through Flow Design Bureau AS, in controller programming that can be adapted into the thesis work.

-- ” --

Within 14 days of receiving the written text on the diploma thesis, the candidate shall submit a research plan for his project to the department.

When the thesis is evaluated, emphasis is put on processing of the results, and that they are presented in tabular and/or graphic form in a clear manner, and that they are analyzed carefully.

The thesis should be formulated as a research report with summary both in English and Norwegian, conclusion, literature references, table of contents etc. During the preparation of the text, the candidate should make an effort to produce a well-structured and easily readable report. In order to ease the evaluation of the thesis, it is important that the cross-references are correct. In the making of the report, strong emphasis should be placed on both a thorough discussion of the results and an orderly presentation.

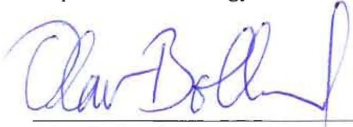
The candidate is requested to initiate and keep close contact with his/her academic supervisor(s) throughout the working period. The candidate must follow the rules and regulations of NTNU as well as passive directions given by the Department of Energy and Process Engineering.

Pursuant to “Regulations concerning the supplementary provisions to the technology study program/Master of Science” at NTNU §20, the Department reserves the permission to utilize all the results and data for teaching and research purposes as well as in future publications.

One – 1 complete original of the thesis shall be submitted to the authority that handed out the set subject. (A short summary including the author’s name and the title of the thesis should also be submitted, for use as reference in journals (max. 1 page with double spacing)).

Two – 2 – copies of the thesis shall be submitted to the Department. Upon request, additional copies shall be submitted directly to research advisors/companies. A CD-ROM (Word format or corresponding) containing the thesis, and including the short summary, must also be submitted to the Department of Energy and Process Engineering

Department of Energy and Process Engineering, 10.12. 2010



Olav Bolland  
Department ~~Manager~~ HEAD



Morten Kjeldsen  
Academic Supervisor

Research Advisors:

Håkon Hjort Francke Flow Design Bureau AS



# Preface

This thesis has been written and researched at the Waterpower Laboratory at NTNU in the spring of 2011. It deals with the prospects of morphing skin and structures in a hydroturbine context.

The research could not have been carried out without the practical help from PhD candidate Mette Eltvik, PhD Håkon Hjort Francke, scientific assistant Bjørn Winther Solemslie and many others. My supervisor, associate professor Morten Kjeldsen, has provided valuable insight and knowledge, as well as direction. He has also given me an interesting job!

The construction of my practical test rig would not have been possible without the help and experience of Joar Grillstad and the other technicians at the laboratory.

---

Jarle Vikør Ekanger  
Trondheim, June 9, 2011





# Abstract

This thesis deals with the application of morphing skin and structure technology in a hydroturbine context. The work has been divided into two parts; construction of a demonstration rig and CFD calculations assessing the concept of camber morphing of guide vanes.

Five rubber 'morphing bumps' reduce the intensity of vortex shedding behind a cylinder in an open flow of water. The bumps are made by a rubber bellows placed in a perforated stainless steel pipe. Their size is controlled by air pressure, and the option of reducing them to a neutral state is present. A control software has been designed using Labview, allowing manual and automatic (model predicted flow control) operation, as well as logging of measurements. The tests show that the bumps are capable of reducing vortex intensity by approximately 25%.

CFD simulations has been performed on a Francis turbine section to determine if altering the camber of guide vanes at different loads can have a beneficial effect to the performance and wear characteristics. The simulations resulted in a dataset consisting of steady state and transient simulation results from 28 combinations of camber and wicket gate opening. The results did not establish that camber morphing can increase efficiency, but neither did they reject it completely. It has been shown that for small cambers up to 2%, the gains from increased lift far outweigh increased drag at part loads.



# Samandrag

Denne rapporten tek for seg bruk av adaptive overflatar og strukturar i vassturbin-samanheng. Arbeidet har vore todelt; ein praktisk demonstrasjonsrigg og CFD-simulering som tok for seg krummingsadaptive leieskovlar.

Fem 'gummiknølar' reduserer intensiteten i virvelavløysinga bak ein sylinder i ei fri overflate-strømning. Knølane vert danna av ein gummibelg som er plassert inne i eit perforert stålrøyr. Storleiken deira kan regularast ved hjelp av lufttrykk, og dei kan trekkast tilbake til ei nøytral tilstand om ønska. Eit kontrollprogram har vorte utvikla i LabView, som tillet manuell og automatisk (modellstyrt strømningskontroll) styring, og som lagrar data frå tilstandsmålingane. Testar av riggen viser at intensiteten til dei avløyste virvlane kan reduserast med omlag 25%.

CFD-simuleringar har vorte utførte på ein Francisturbinseksjon for å avgjere om adaptiv leieskovlskrumming kan føre med seg auka yting og redusert slitasje. Simuleringane produserte eit datasett som består av 28 kombinasjonar av leieskovlskrumming og leieapparatsopning. Resultata korkje bekreftar eller avkreftar at adaptiv leieskovlskrummingkan auke ytinga, men for det gjeldande datasettet har det vist seg at adaptiv krumming ikkje kunne auke ytinga. Det har altså komme fram at for små krummingar, opp til 2%, fører auka løft til mykje større positiv ytingsendring enn auka vassmotstand kan motvirke.



# Contents

List of Figures . . . . .	ix
List of Tables . . . . .	x
List of Equations . . . . .	x
Nomenclature . . . . .	xi
<b>1 Flow control in a hydropower context</b>	<b>1</b>
<b>2 Summary of theory and work</b>	<b>3</b>
2.1 Francis turbines - basic theory . . . . .	3
2.2 The flow past guide vanes and stay vanes . . . . .	5
2.2.1 Separation . . . . .	6
2.2.2 Blade passing frequencies . . . . .	7
2.3 Draft tube swirl . . . . .	7
2.4 Secondary flows in hydro turbines . . . . .	8
2.4.1 Wakes . . . . .	8
2.4.2 Leakage flows . . . . .	9
2.4.3 Vibrations caused by von Kármán vortices . . . . .	9
2.5 Vortex shedding in body wakes . . . . .	13
2.6 Methods for control of Vortex-Induced Vibrations . . . . .	14
2.6.1 Passive control . . . . .	14
2.6.2 Active control . . . . .	15
<b>3 Morphing structures and skins</b>	<b>17</b>
3.1 Introduction . . . . .	17
3.2 Overview of work on morphing structures and skins . . . . .	18
3.2.1 Skin-covered substructures . . . . .	18
3.2.2 Morphing skins . . . . .	20
3.2.3 Continuous substructures . . . . .	21
3.3 State-of-the-art . . . . .	22
3.4 Possible hydroturbine application . . . . .	22
3.4.1 Guide vane morphing . . . . .	22
3.4.2 Leakage flow inhibition . . . . .	23
3.4.3 Swirl flow inhibition . . . . .	23
3.4.4 Modes of operation . . . . .	23
<b>4 Rig experiment</b>	<b>25</b>

4.1	Introduction to the rig design . . . . .	25
4.2	Design objectives . . . . .	25
4.3	The rig design . . . . .	27
4.3.1	The pipe . . . . .	27
4.3.2	The pressurized rubber bellows . . . . .	27
4.3.3	Velocity measurement . . . . .	28
4.3.4	Vortex measurement . . . . .	28
4.3.5	Control interface . . . . .	28
4.3.6	The governor . . . . .	30
4.3.7	Troubleshooting . . . . .	30
4.4	Rig operation . . . . .	31
4.5	Rig test measurements . . . . .	32
4.5.1	First test measurements . . . . .	32
4.5.2	Second test measurements . . . . .	34
4.5.3	Discussion: Rig test results . . . . .	36
4.6	Autocontrol mode tests . . . . .	38
<b>5</b>	<b>CFD</b>	<b>43</b>
5.1	Governing equations and models . . . . .	43
5.2	Simulations . . . . .	44
5.2.1	Meshing . . . . .	45
5.2.2	Case overview . . . . .	46
5.3	Expected simulation results . . . . .	46
<b>6</b>	<b>CFD Results</b>	<b>49</b>
6.1	Performance data . . . . .	49
6.2	Torque variations . . . . .	50
6.3	Wake sizes . . . . .	51
6.4	Forces on the guide vane . . . . .	54
6.5	Discussion: CFD results . . . . .	56
6.5.1	Morphing guide vane requirements . . . . .	60
<b>7</b>	<b>Conclusion and further work</b>	<b>67</b>
<b>Appendices</b>		
<b>A</b>	<b>Demonstration rig - Technical details</b>	<b>75</b>
<b>B</b>	<b>Experimental work</b>	<b>77</b>
B.1	First test measurements . . . . .	77
B.2	Second test measurements . . . . .	77

# List of Figures

2.1	Francis turbine . . . . .	4
2.2	Energy distribution in Francis Turbine . . . . .	4
2.3	Velocity diagram for Francis Turbine . . . . .	5
2.4	Flowlines and pressure around hydrofoil . . . . .	6
2.5	Experimental work by R. M. Donaldson . . . . .	10
2.6	Suction Vortex Airfoil . . . . .	11
2.7	Ausoni: Cavitation in wake . . . . .	13
2.8	Bumped cylinder . . . . .	15
3.1	The Monner 'finger concept' . . . . .	20
4.1	Demo rig; upstream view . . . . .	26
4.2	Demo rig; modes of operation . . . . .	29
4.3	The rig/lab configuration . . . . .	31
4.4	Results from Test 1-3 . . . . .	32
4.5	Results from Test 1-4 . . . . .	33
4.6	Results from Test 1-5 . . . . .	33
4.7	Results from Test 2-1 . . . . .	35
4.8	Results from Test 2-4 . . . . .	35
4.9	Results from Test 2-6 . . . . .	36
4.10	Autocontrol mode rig test . . . . .	39
4.11	Autocontrol detail . . . . .	40
4.12	Autocontrol detail . . . . .	40
5.1	Guide vane mesh . . . . .	45
5.2	Mesh overview . . . . .	46
6.1	Turbine performance . . . . .	51
6.2	Max/Min Torque . . . . .	52
6.3	Torque variation . . . . .	53
6.4	Wake profiles . . . . .	54
6.5	Wake widths . . . . .	55
6.6	Viscous drag on guide vane . . . . .	56
6.7	Comparison of wakes . . . . .	57
6.8	Guide vane torque . . . . .	58
6.9	Guide vane pressure drag . . . . .	59

6.10	Guide vane lift . . . . .	60
6.11	Turbine pressure . . . . .	61
6.12	Total drag on guide vane . . . . .	63
6.13	Turbine velocity field . . . . .	64
6.14	Torque time series . . . . .	65
A.1	System schematic . . . . .	76
B.1	Results from Test 1-1 . . . . .	78
B.2	Results from Test 1-2 . . . . .	79
B.3	Results from Test 1-3 . . . . .	80
B.4	Results from Test 1-4 . . . . .	81
B.5	Results from Test 1-5 . . . . .	82
B.6	Results from Test 1-6 . . . . .	83
B.7	Results from Test 2-1 . . . . .	84
B.8	Results from Test 2-2 . . . . .	85
B.9	Results from Test 2-3 . . . . .	86
B.10	Results from Test 2-4 . . . . .	87
B.11	Results from Test 2-5 . . . . .	88
B.12	Results from Test 2-6 . . . . .	89

# List of Tables

4.1	Flow control concept test #1 - Results overview . . . . .	34
4.2	Flow control concept test #2 - Results overview . . . . .	37
5.1	An overview of the different NACA profiles and angles of attack investigated. . . . .	47
6.1	An overview of the performance results . . . . .	50
6.2	An overview of the guide vane force results . . . . .	62



## List of Equations

2.1 Hydraulic efficiency of a Francis turbine . . . . .	3
2.2 Momentum equation at a wall . . . . .	7
2.3 Runner blade excitation frequency . . . . .	7
2.4 Guide vane excitation frequency . . . . .	7
2.5 Strouhal formula . . . . .	13
2.6 Gongwer's corrected Strouhal formula . . . . .	13
2.7 Definition of $\delta_d$ . . . . .	14
6.1 Total head . . . . .	49
6.2 Turbine power . . . . .	49
6.3 Equation name . . . . .	49
6.4 Wake profile conditioning equation . . . . .	51
6.5 Normalization equations for U and y . . . . .	52
6.6 Viscous Drag . . . . .	52
6.7 Drag coefficient . . . . .	53



# Nomenclature

$\delta_d$	Turbulent BL displacement thickness	m
$\delta_v$	Virtual displacement thickness	m
$\dot{m}$	Mass flow rate	kg/s
$\eta_h$	Hydraulic efficiency	-
$\mu$	Dynamic viscosity	Pas
$\omega$	Angular velocity	rad/s
$\rho$	Density	kg/m <sup>3</sup>
$\sigma$	Cavitation index	-
$\tau$	Shear stress	Pa
$\zeta$	Damping ratio	-
$A$	Projected area	m <sup>2</sup>
$A_a$	Activated mode vortex amplitude (st. dev)	V
$A_n$	Neutral mode vortex amplitude (st. dev)	V
$b$	Arbitrary width	m
$C_d$	Drag coefficient	-
$C_l$	Lift coefficient	-
$c_{u1}$	Tangential comp. of absolute flow velocity at inlet	m/s
$c_{u2}$	Tangential comp. of absolute flow velocity at outlet	m/s
$d$	Diameter	m
$f$	Vortex shedding frequency	Hz
$F_D$	Drag	N
$F_L$	Lift	N

$f_r$	Runner blade excitation frequency	Hz
$f_{conditioning}$	Velocity wake conditioning function	-
$f_{gv}$	Guide vane excitation frequency	-
$g$	Acceleration of gravity	m/s <sup>2</sup>
$H$	Total head	m
$h/\lambda$	Wave height to length ratio	-
$L$	Characteristic body length	m
$m^*$	Mass ratio	-
$M_z$	Shaft torque	J
$n$	Runner speed	r/min
$P$	Power	W
$p$	Static pressure	Pa
$p_{tot}$	Total pressure	Pa
$Q$	Flow rate	m <sup>3</sup> /s
$St$	Strouhal number	-
$U$	Freestream velocity	m/s
$u$	Local velocity	m/s
$u_1$	Tangential velocity of runner at inlet	m/s
$u_2$	Tangential velocity of runner at outlet	m/s
$u_n$	Normalized velocity	-
$x$	Streamwise position	m
$x_w$	Streamwise distance from trailing edge	m
$y$	Spanwise position	m
$y_n$	Normalized spanwise position (in wake)	-
$Z_g$	Number of guide vanes	-
$Z_r$	Number of runner blades	-





# Chapter 1

## Flow control in a hydropower context

Flow control is inherently part of hydropower turbines, in the sense that control surfaces such as the guide vanes are used to govern the primary flow patterns. However; guide vane, stay vane and runner designs can not take into account all adverse flow effects occurring at off-design operation. These effects generally involve vortices, and in draft tube context may also include cavitation, caused by adverse flow conditions. Another important issue is leakage flows, that to some extent are unavoidable. These secondary flow fields are often central to the reduced performance of hydroturbines at off-design operating conditions.

The base design of course aims to minimize such secondary flows, but only so much can be done. An implement to suppress an adverse flow characteristic at one operation point might cause increased losses at another operation point.





# Chapter 2

## Summary of theory and work

### 2.1 Francis turbines - basic theory

The Francis turbine is a reaction turbine; the runner converts both kinetic and potential energy to axial torque. The turbine consists of a spiral casing, stay vanes, guide vanes, a runner and a draft tube. The guide vanes control the flow and are the only movable parts, apart from the runner. Francis turbines exhibit better best-point efficiency than Pelton and Kaplan turbines, but in a narrow flow range. The shape of the runner is determined by flow and head.

The flow is controlled by adjusting the angle of the the guide vanes. The runner converts potential energy and the kinetic energy from the tangential velocity component to torque on the runner shaft. The meridional velocity increase slightly through the turbine to fullfill continuity. This acceleration cause a global pressure and suction side on stay and guide vanes [2]. The draft tube is a diffuser, where most of the velocity is regained as pressure (see figure 2.2).

The efficiency of the turbine is the ratio of converted energy to available energy at the inlet. Euler defined the hydraulic efficiency using velocity components at the inlet and outlet.

$$\eta_h = \frac{u_1 c_{u1} - u_2 c_{u2}}{gH} = 2(\underline{u}_1 \underline{c}_{u1} - \underline{u}_2 \underline{c}_{u2}) \quad (2.1)$$

Velocity components at various stages of the turbine are effective in describing the functions of the different components, see figure 2.3. Note how velocity deficiency in the wake of the guide vane will momentarily alter the direction of  $w_1$ , causing an oscillating force on the runner blade inlet. This, of course, is a frequency excitation source. At the best efficiency point, BEP,  $w_1 = *w_1$  is parallell to the runner inlet, thus minimizing impact shocks. These conditions can be summarized for the three main regimes of operation, assuming symmetric guide vanes:



Figure 2.1: Francis turbine cut-away. Guide vanes (yellow) are at full opening. The inlet of the draft tube can be seen in the lower right corner. Spiral casing and stay vanes upstream of guide vanes (not clearly visible). Source: Wikimedia Commons[1]

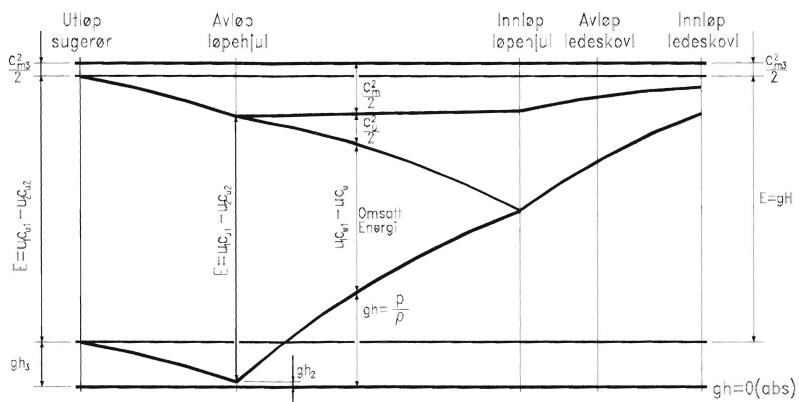


Figure 2.2: The Energy distribution in a Francis turbine. From [3].

Part load

- Runner inlet angle too small.
- Pressure difference on the guide vane from angle of attack is of the same direction as the global pressure difference.

BEP

- Runner inlet angle is correct.
- No pressure difference on the guide vane from angle of attack (assuming stay vane angles are designed for BEP), but still an adverse global pressure difference.

Full load

- Runner inlet angle too large, water hits suction side of runner inlet.
- Pressure difference on the guide vane from angle of attack is opposite to the direction of global pressure difference.

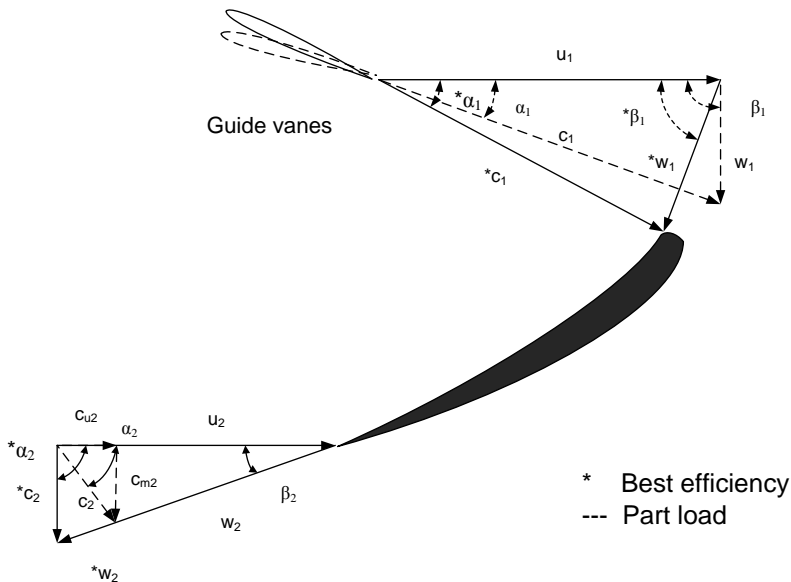


Figure 2.3: The velocity components of guide vane and runner vane inlets/outlets.

## 2.2 The flow past guide vanes and stay vanes

The application of Bernoulli's equation along a streamline illustrates that the pressure decreases in accelerated areas and increases in decelerated areas. Thus the

alteration of flow around a body cause changes to the velocity and pressure. These changes are dependent on the flowfield. From this it is apparent that the pressure distribution around the body can be altered by changing it's shape and thus the local flowfield. The shape of a hydrofoil can be described by it's camber line and relative thickness. The camber line describes a line running halfway between the foil's upper and lower surface. By curving the camber line, a foil that has lift at zero incidence angle is achieved. The lift is due to a pressure difference between the upper and lower side of the foil, induced by different degrees of acceleration. White [4] states that the flow off the trailing edge of the foil is approximately parallel to the camber line.

The cascade of guide vanes, also called the wicket gate, forms a constriction to the flow area. As a result there is a subsequent acceleration and deceleration of the flow as it passes the guide vanes. Additionally a 'global pressure gradient' is set up as the flow is accelerated in the meridional direction when it flows towards the turbine shaft (the cross-section decrease). The use of camber to reduce pressure difference across the guide vane has been proposed by Antonsen [5]. Eide [2] shows that the pressure difference results in leakage flows through the clearance gaps between the guide vanes and the turbine head covers. This global pressure difference decrease as guide vane opening is increased. Thus leakage could be said to be a major contributor to efficiency loss at part load.

Vortices are shed regularly at the trailing edge of foils. These vortices act on the blade with alternating direction, exciting vibrations at their shedding frequency. The subject is covered in chapter 2.5.

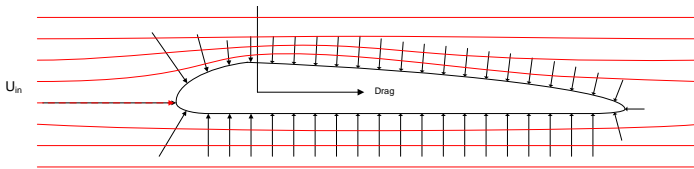


Figure 2.4: Sketch of the flowlines and wall pressures acting on a hydrofoil. Note that the pressure side is under the foil.

## 2.2.1 Separation

The premise for flow separation is a positive pressure gradient in the flow direction, termed an adverse pressure gradient. For pressure gradients less than zero, separation can not occur. In the case of flow past hydrofoils, Bernoulli's equation shows that the local pressure gradient may be positive downstream from the thickest section of the foil, provided the deceleration due to increased cross-sectional area is larger than the acceleration caused by decreasing radius. The governing equation

is the momentum equation at the wall.

$$\frac{\partial \tau}{\partial y}|_{wall} = \mu \cdot \frac{\partial^2 u}{\partial y^2}|_{wall} = -\rho U \frac{dU}{dx} = \frac{dp}{dx} \quad (2.2)$$

Typically, the pressure gradient and transverse velocity gradient will develop along the wall. If it reaches the point where  $\tau_{wall} = 0$  the flow will separate. The flow will tear away from the wall, and a backflow region develops downstream [4]. This causes a loss of lift to the hydrofoil (a stall), and naturally also an increased wake width.

### 2.2.2 Blade passing frequencies

Rotor-stator interactions cause vibrations in guide vanes and runner blades. The blades are respectively exposed to an excitation as they are passed by or pass by a neighbouring blade [5].

The frequency a runner blade is exposed to is proportional to the number of guide vanes and the runner speed.

$$f_r = \frac{nZ_g}{60} \quad (2.3)$$

The frequency a guide vane is exposed to by the runner is proportional to runner speed and number of runner blades.

$$f_{gv} = \frac{nZ_r}{60} \quad (2.4)$$

## 2.3 Draft tube swirl

The author presented a project thesis on the subject of swirling draft tube flow, in which experimental results suggesting pressure fluctuations in the draft tube is a direct result of the tangential velocity component at the draft tube inlet setting up an excentric vortex in the draft tube [6]. The tangential component is a result of the fixed runner blades' inability to adjust to a varying discharge in a Francis turbine . Thus the component is present at both part load and full load. The swirl has been known as the cause of large power fluctuations as far back as 1940 [7], and a solution capable of being installed in existing machinery has been developed at NTNU Vannkraftlaboratoriet [8].

## 2.4 Secondary flows in hydro turbines

So far, a description of the basics of a Francis turbine and some of the flow phenomena that occur in it has been described. This section of the chapter is dedicated to specific secondary flows occurring in various parts of the turbine.

### 2.4.1 Wakes

In his Doctoral Thesis *Unsteady flow in wicket gate and runner with focus on static and dynamic load on runner* [5], Øyvind Antonsen describes some of the problems related to secondary flow phenomena in the wicket gate to runner interaction of Francis turbines. Referring to his article *CFD simulation of von Karman vortex shedding* [9] he points out that the vortex street behind guide vanes has high frequency and low amplitudes, due to the thin trailing edge. Thus, the shedding in itself rarely cause problems, but there might still be problems related to the runner blades entering the wakes. A tangentially varying pressure field, caused by the pressure and suction sides on the guide vanes, add to this. The fluctuating force experienced by the runner blades is thought to be the main reason for cracking in Francis runners [10]. Antonsen showed by experiment that shaping the guide vanes in a manner such that local pressure and suction sides counteracts the global ones is possible, thus reducing the pressure variations experienced by the runner. It did not alter the losses measured and consequently would not affect turbine efficiency. Maclean and Decker [11] investigated flow past symmetric and cambered NACA0012 foils using the vortex blob method and found that the symmetric foil simulations followed thin foil theory, while cambered foils exhibited larger lifts and separated later. This suggests that if a morphing camber guide vane is realisable, smaller deflections of the trailing edge is necessary and that a reduction of wake width is possible.

The importance of von Kármán vortex streets on runner blade cracking is also discussed by Aronson et al in the article *Experience in operating hydraulic structure and equipment of hydroelectric stations* [12]. This article focuses on the cracking in stay vanes, concluding that the main reason for cracking is the vortex induced vibrations due to von Kármán vortex shedding. The authors argue that in a corrosive environment there is no fatigue limit, and that the breaking amplitude decrease continually as number of loading cycles increase. Thus, vibrations may reduce the safety factor for breaking considerably, and eventually cause a vane failure. Good experience with dovetailing trailing edges is reported, see page 10 for more on dovetails.

*Analysis of separated flow in hydro machines*[13] by Arpad A. Fay raises the question on whether rotating stall occur in hydro turbines. Stall is defined as a boundary layer separation that does not re-attach to the wall. A rotating stall is a situation where a stall moves from blade to blade in a foil cascade. The phenomenon is known to cause back-flow in axial pumps. The mechanism causing the stall to

rotate is the blocking effect of the stalled region, forcing fluid to divert and thus induce stall on the next foil. Arpad then proceeds to suggest that a rotating stall on the inlet of a Francis turbine's runner blades may be the cause of the much discussed draft tube vortex rope, that may cause large power fluctuations. He points out that this theory is not in opposition to the precession theory, the theory that is commonly accepted to explain stabilization of the vortex rope. If rotating stall plays a role in the formation of the vortex rope, it becomes apparent that control of secondary flows at the runner inlet may be vital to widening the Francis turbine stable operation range.

The shedding of von Kármán vortices from the trailing edges of the runner blades may also cause vibration related problems. These issues are explained in chapter 2.5

### 2.4.2 Leakage flows

The pressure difference from the pressure side to the suction side of a guide vane cause a leakage flow to penetrate the narrow clearance gap between the guide vane and the turbine casing. In *Numerical analysis of the head covers deflection and the leakage flow in the guide vanes of high head Francis turbines* [2] Sølvi Eide shows that such leakage flows are a major contribution to the loss in Francis turbines. The flows disturb the main flow in the guide vane cascade, causing vortices and deviations from the targeted inflow angle to the runner. A minimum of clearance gap is necessary to prevent grinding during unpressurised operation, and this gap is increased by the pressure present during normal operation.

### 2.4.3 Vibrations caused by von Kármán vortices

A few articles written in the 50's and 60's, on the subject of flow induced vibrations lay out the basics of this field. Such old articles usually describe subjects that have been covered more thoroughly later on, but serve well as the basis for literature searches into newer material. Some of these old articles, as they are published in for instance *The Proceedings of the ASME*, include peer reviews, adding a deeper perspective to the article.

Modern equipment and computers have greatly increased the potential for detailed research on the phenomena connected to von Kármán vortex streets. Investigations are still being done on bluff cylinders, that being an easy geometry on which to try out methods for attenuating the vibration exciting forces on the immersed body. The present focus is mainly on methods of controlling the development of the boundary layer, to minimize drag and vibrations caused by the vortex street.

In the article *Hydraulic-Turbine Runner Vibration*[14], R. M. Donaldson describes investigations into the effect of different trailing edge geometries on Francis turbine runner vibrations. The article focuses on vibrations presumed to stem from forces

excited by shedding of von Kármán vortices from the trailing edge of the runner blades. His observations are based on field experience from several plants in the US and laboratory experiments. Donaldson performed laboratory tests to determine the effects of different trailing edge shapes on vortex shedding characteristics. The results, shown in figure 2.5 suggest that the magnitude of the von Kármán vortex street pressure pulsations may be significantly reduced by changing the shape of the trailing edge. The shedding frequency was not found to change significantly through changing the edge geometry, which is in accordance with the assumption that the Strouhal number is fairly constant (for similar body shapes, see chapter 2.5).

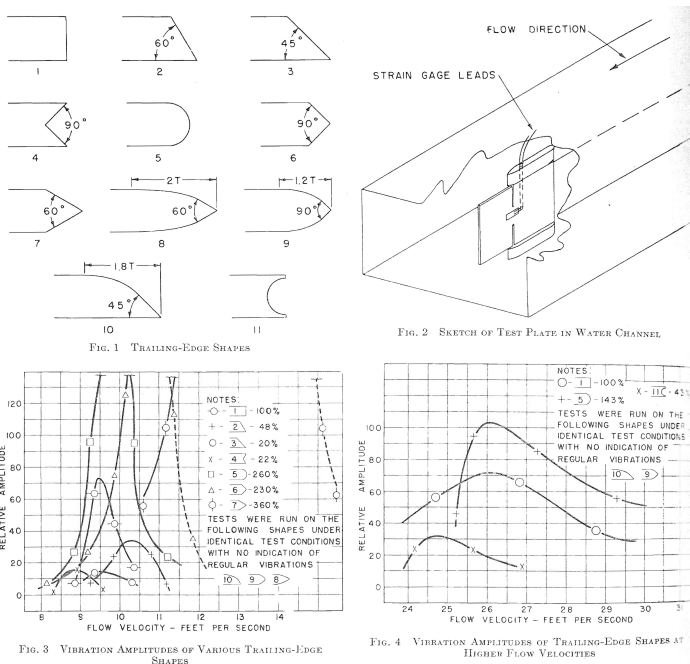


Figure 2.5: The experiments performed by Donaldson investigated different trailing edges on aluminium plates in a water channel. The different shapes and their vibration amplitudes relative to a truncated edge are documented. Note that asymmetry and the use of grooves display attenuation, while symmetric tapering amplifies the amplitude. From [14]

Donaldson’s final results are field implementations of new trailing edge geometries. Trailing edges of type 10 and 11 (‘dovetail’) in figure 2.5 were applied to two of the three units at the site. Later inspection revealed chipping on the trailing edge of the unit not refurbished, slight cavitation damage in the grooves of the unit on which the type 11 edge was applied, and no visible damage to the unit on which edge type 10 was applied.



In the review of Donaldson's article, D. C. Hazen<sup>1</sup> and C. P. Kittredge<sup>2</sup> claim that the vortex street can be eliminated by achieving a stabilized vortex along the trailing edge through suction. They claim to have observed that this can be achieved solely by the presence of an adequate parallel velocity component at the trailing edge. This has been achieved on the *suction vortex airfoil* presented in figure 2.6.

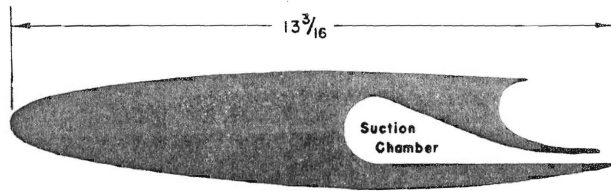


FIG. 5 SUCTION VORTEX WING

Figure 2.6: The Hazen-Kittredge suction vortex airfoil. From [14]

Jaski<sup>3</sup> suggests that the attenuating effect on runner blade vibration may be the result of the two vortices from opposite sides quenching each other, rather than alternating. This eliminates the fluctuating force on the blade, that excites vibrations (further described in the next paragraph). W. J. Rheingans<sup>4</sup> rejects the claims of G. D. Johnson<sup>5</sup> that all vibration issues are audible and thus detectible without the equipment used by Donaldson. He claims vibrations may be present in parts of the system, without propagating to accesible parts. He further notes that the findings of Donaldson represent a better alternative than the previously sole solution; to install struts between the runner blades, a practice that merely inhibit the blades ability to oscillate. Vencill<sup>6</sup> enclose his own good experience with edge type 11, as well as experience with cavitation pitting that caused the discharge edge to approach the shape of edge type 10.

Heskestad and Olberts add valuable understanding to the results presented by Donaldson in the article *Influence of Trailing-Edge Geometry on Hydraulic-Turbine-Blade Vibration Resulting from Vortex Excitation* [15]. Like Donaldson, they investigated the influence of trailing edge geometry on the amplitude and frequency of hydrofoil vibration. However, a more systematic approach to geometries is applied, dividing the edges into asymmetrically tapered edges, symmetrically tapered edges and a single grooved discharge edge. Measurements include vibration frequency, amplitude and vortex strength. Additionally, more acute angles were investigated

<sup>1</sup> Assistant Professor of Aeronautical Engineering, Princeton University

<sup>2</sup> Associate Professor of Mechanical Engineering, Princeton University

<sup>3</sup> Engineer-in-charge, Pump Turbines, Allis-Chalmers Manufacturing Company

<sup>4</sup> Manager, Hydraulic Department, Allis-Chalmers Manufacturing Company

<sup>5</sup> Chief Hydraulic Engineer, S. Morgan Smith Company

<sup>6</sup> Union ELectric Company of Missouri

than by Donaldson. The key results presented in the article is that for the more acute angles on symmetric edges, the amplitudes of vibration decrease, thus refuting the findings of Donaldson; that symmetrically tapered edges cause an increased amplitude of vibration. The statement is still true for angles similar to those investigated by Donaldson, but the tendency is reversed as the edge angle becomes more acute. The results agree with Donaldson not being able to detect steady vibrations for some of his geometries. Heskestad and Olberts discuss these results more thoroughly, and points out that the reduction of vibration amplitude corresponds to a reduction of distance between the two separation points. This leads to an overlap of oppositely oriented vortices, in which the two vortices to some degree cancel each other out. For the cases of increased vibration, the separation points remain at the corners of the tapering edge, but now separated by a wall that allows each vortex to develop further before entering the vortex street. For the case of a groove in the trailing edge, a stationary slog of rotating water oscillates in opposition to the vortices shed, reducing their size without reducing the vortex strength. Heskestad and Olberts emphasise the understanding that the ratio between boundary layer thickness and distance between separation points, as well as the physical shielding between the separation points, are the vital elements to control in order to reduce vibration problems on hydrofoils and the size of the wakes behind them. Their results also show that though vibration frequency increase linearly with flow velocity (with the exception of around the resonance frequency), the rate of increase is not equal for all edge geometries.

The article *A Study of Vanes Singing in Water*[16] by C. A. Gongwer is one of the earlier articles on flow induced vibrations, in which the methods and results may be less subject to quantitative quality than in the formerly mentioned articles. Yet there are some important results, including that the shedding of vortices from the trailing edge does not follow the same Strouhal law that applies for flow around bluff cylinders. Gongwer adds a correction to the Strouhal formula by adding a virtual thickness based on the boundary layer thickness to the thickness of the body.

Ausoni et al has published a number of articles on the vortex shedding behind hydrofoils. The article *Vortex shedding from blunt and oblique trailing edge hydrofoils* [17], in which the oblique trailing edge is termed a 'Donaldson cut', seeks to further explain the mechanism that attenuate the vibrations. Ausoni et al perform their tests on NACA0009 hydrofoils, one with a 30° oblique trailing edge, and one truncated. The results confirm the findings of Donaldson and Heskestad and Olberts, in regards to trailing edge geometry. Lock-in, a situation where the vortex shedding frequency is locked to the natural frequency of the hydrofoil, is observed to shift towards higher frequencies for the oblique edge. High speed visualization shows a disorganisation of the vortex street, resulting in an attenuation of the vibration exciting transversal force. Furthermore, the wake is observed to have a smaller velocity deficit, and more turbulence, for the oblique edge. More precisely, there is a phase shift of the two vortex sheets leading to pairing and partial destruction of the vortices, like Heskestad and Olberts suggested. An important find is presented

in *Cavitation Influence on von Kármán Vortex Shedding and Induced Hydrofoil Vibrations* [18], that should be taken into consideration during experiments; it was found that the vortex shedding frequency increased by up to 15%, see figure 2.7. At the same time, the vortex advection velocity increased, and the vortex spacing decreased. All this was accompanied by increased vibration. This has been successfully utilized to control hydro-elastic coupling (i.e. lock-in) by allowing a sufficient amount of cavitation to develop.

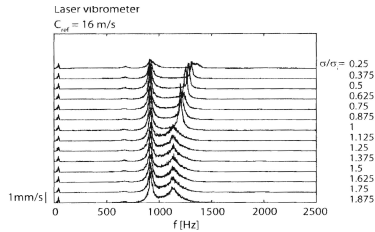


Figure 2.7: The effect of cavitation can be seen on vortex shedding frequency in lock-off conditions. Cavitation appears for  $\frac{\sigma}{\sigma_i} \leq 1$ . The natural frequency of the foil was found to be 900 Hz. From [18]

## 2.5 Vortex shedding in body wakes

The shedding of vortices behind immersed bodies is named after Theodore von Kármán, he described the viscous flow past a cylinder [19]. The wake is assymetrical, with vortices shed alternately from each side of the the body. Von Kármán explained that the alternating vortex shedding is a stable configuration for vortex pairs [20]. As the shedding of vortices oscillate from side to side, the body is subjected to an oscillating force perpendicular to the flow direction. The dimensionless frequency at which the vortices are shed from cylinders is called the Strouhal number:

$$St = \frac{fL}{U} \quad (2.5)$$

It has been shown that the Strouhal number is constant at about 0.2 for a range of Reynolds numbers  $10^2 \leq Re \leq 10^7$ . Gongwer [16] made a correction to Strouhal's formula for flow past hydrofoils:

$$St = \frac{f \cdot (L + \delta_v)}{U} \quad (2.6)$$

Where  $\delta_v$  is an empirically determined fraction 0,643 of the turbulent boundary

layer displacement thickness  $\delta_d$ , defined as

$$\delta_d = \frac{1}{8} \cdot \frac{0,37L}{Re_L^{\frac{1}{5}}} \quad (2.7)$$

It is notable that the value of the Strouhal number differs from 0.2, but has been observed to be constant for a range of Reynolds numbers. Hermod Brekke[3] present a formula not unlike Gongwer. Unlike Gongwer, Brekke has introduced a constant additional displacement thickness of 0,56 mm.

## 2.6 Methods for control of Vortex-Induced Vibrations

### 2.6.1 Passive control

Ausoni et al has written a report called *Hydrofoil roughness effects on von Kármán vortex shedding* [21]. The subject of the report is an investigation into the effect of glueing a strip of 125  $\mu\text{m}$  sand to each side of the hydrofoil's leading edge. The object of the added roughness is to force the transition to a turbulent boundary layer at the leading edge. Results show that the shedding frequency is reduced for the rough hydrofoil, implying a thinner boundary layer [16]. However, the vibration amplitudes are larger, due to a higher degree of spanwise organization. This spanwise organization stems from the forced transition to a turbulent boundary layer on the rough leading edge.

Owen and Bearman describe a method using wavy separation lines to reduce vortex shedding and drag. In their initial experiments [22], they studied flow past plates and rectangular bodies with a sinusoidal shape or leading edge. The results showed up to 30% drag reduction, and complete suppression of vortex shedding, the mechanism being a distortion of the vortex shedding. They report that from a threshold wavelength to body diameter ratio and wave steepness they observe no shedding. There is, however, a gradient transition from full to no vortex shedding. In a later article [23] the concept has been further developed, in the form of a cylinder with bumps (figure 2.8). The results show that there is a gradual convergence on drag reduction as the wave steepness is increased. Investigations into bump spacing has not been covered thoroughly, but the current design allows bumps to be placed in a spiralling manner, to eliminate flow direction dependency.

Ausoni's experiment is a good example of how boundary layer control affects flow on and behind a body. The effect described is the opposite of that described by Owen and Bearman, but the mechanism is essentially the same; manipulation of boundary layer development. Thus, the 3D characteristics of the vortex street has a big influence on the pressure fluctuations. Szepessy and Bearman [24] investigated this. They found that spanwise phase shifts reduce the size of RMS pressure fluctuation

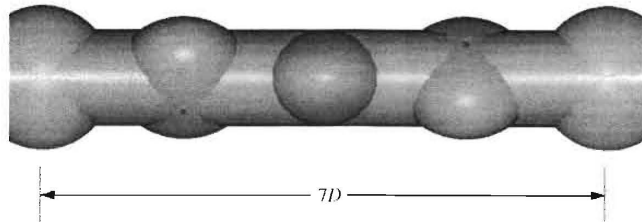


Figure 2.8: The bumped cylinder from Owen and Bearmans experiments. Source: [23]

values on the body. They further report that a single disturbed vortex can have a quite large influence on averaged fluctuations.

Kumar [25] gives an overview of passive control methods, including the use of vortex generators, perforated shrouds, streamlining and adding of structures such as foils or bumps on the cylinder. Some of these methods consist of adding a structure that streamlines the structure, effectively changing the shape towards that of an air- or hydrofoil. Another important group mentioned is the helical strakes, commonly seen on e.g. smokestacks. Perforated shrouds affect entrainment, thus affecting the vortex shedding. Vortex generators energize the boundary layer, thus reducing its growth and postponing separation.

### 2.6.2 Active control

Huang [26], Blevins [27] and Williams and Zhao [28] describe methods that reduce vortex shedding through use of sound. Both Blevins and Williams and Zhao installed speakers in the walls of test tunnels, directed towards a cylinder. It was found that when applying sound with a frequency equal to the vortex shedding frequency the frequency spectrum would show a decreasing bandwidth when the sound intensity increased. In the same manner, it was shown that vortex shedding frequency could be shifted towards the natural frequency if the imposed sound was sufficiently intense. This method cause a better spanwise homogeneity to the vortex sheddings. Huang introduces the sound to the flow through a slit in the cylinder, thus directly affecting the boundary layer. The experiments show that a single slit, positioned to one side of the center line, can suppress vortex shedding for a range of Reynolds numbers from  $4 \cdot 10^3$  to  $1.3 \cdot 10^4$ .

Liu et al [29] utilized a micro actuator to control vortex-induced vibrations in a two-cylinder experiment. The actuators are small piezoelectric 'beams', that will vibrate when an alternating voltage is applied. The actuators are embedded in the cylinder walls, thus creating a vibrating section of the wall, near the anticipated separation point. The tests show a 50 to 80% reduction of cylinder vibration energy with actuator vibration. Liu concludes that the effect is best with large actuator

vibration amplitudes; keep in mind that the actuator is very small and lightweight compared to the cylinder.

Chen Zhi-Hua et al [30] use carefully placed magnets and electrodes to create Lorentz forces that attenuate the vibrations. The electromagnetic forces act as suction on the cylinder wall, greatly reducing separation. The experiments showed a significant reduction of the stagnation zone.

Baz and Ro [31] use direct velocity feedback through use of an electromagnetic actuator to reduce flow-induced vibrations. The setup of this experiment consists of an accelerometer from which the signal is amplified and used to operate an electromagnetic actuator. By setting the poles correctly, the actuator oscillates in proportion, but oppositely, to the cylinder. Both accelerometer and actuator is mounted on the free end of a flexible cylinder. Note that this is a way of minimizing fluctuation amplitudes, not to suppress the exciting forces causing it.

## Chapter 3

# Morphing structures and skins

### 3.1 Introduction

The literature studies have shown that areas of concern on matters of efficiency and maintenance/wear is the two inlet cascades and their interaction with the runner. Both Antonsen [5] and Eide [2] point out the unfavorable pressure distribution of the guide vanes.

Looking at the subject of leakage flows it is apparent that their presence is dependent on pressure difference and a gap through which to leak. Thus a flow control method that could eliminate any of these factors would be beneficial. Due to the movement of the guide vanes permanent seals is not an option, but an adjustable seal mechanism could prove helpful. Using camber to mitigate the chordwise pressure difference across the foil has the potential to minimize leakage by reducing the driving force.

The subject of rotor/stator interaction is a little more complex. Antonsen states that both the varying pressure field caused by the pressure and suction sides of the foils and the velocity deficiencies in the guide vane wakes cause fluctuations to the force felt by the runner. Antonsen also showed that camber could effectively alter the pressure distribution. Thus the hope is that camber might reduce both the 'pressure wake' and the velocity wake. To achieve this, one must determine a degree of cambering that simultaneously cancel pressure differences across the foil and reduces the width of the wake behind it, or at the very least reduces one of the parameters, without increasing the other.

Another possible application is runner blade morphing to eliminate tangential velocity components in the draft tube flow. Such an achievement would effectively eliminate the vortex rope, a phenomenon associated with large power swings in Francis turbines at part load [7, 32, 33, 34].

This chapter gives an introduction to the technologies proposed for aeronautical morphing structures and skins (the focal point of present research), and the author's propositions to hydro power application.

## 3.2 Overview of work on morphing structures and skins

Morphing is the smooth alteration of a surface. Changes can have all scales, and may not affect the entire surface in question. An initial distinction should be made between two subgroups of morphing skins; truss work substructures covered by flexible or deployable skins, and continuous structures in which the entire body is build from some material with a morphing ability. Both, however, need to be actuated in some manner. It is imperative to assess the ability of a technology developed for aeronautical applications to be transferred to hydro power conditions.

C. Thill et al give a comprehensive overview - from a voluminous list of references - of the subject in the article *Morphing skins* [35], terming a morphing skin as an aerodynamic surface that covers a morphing substructure. It is pointed out how *biomimetics* - mimicking nature - has been a key inspiration to many engineering milestones. This includes both the Eiffel Tower and the winglets seen on modern passenger aircraft. Another important lesson from nature is the concept of hierarchial structures - structural elements that itself has structures.

### 3.2.1 Skin-covered substructures

This is typically a truss work covered by one or more layer(s) of skin(s). The substructure provides structural strength in the truss intersections, but these are few and relatively far between. Thus the skin needs to be of such a construction that it allows changes in area but at the same time display large out-of-plane strength. Such a skin is able to morph as the substructure nodes moves relative to each other, and at the same time provide a smooth surface to the foil.

Ramrakhiani et al [36] has researched the construction of an aircraft wing concept using tendon-actuated compliant cellular trusses. They exchanged the rotating joints of a traditional truss work with compliant joints, to reduce the transmission of bending moments between trusses. Furthermore, the nodes are connected with tendons, or wires, that can be shortened or lengthened using actuators. Their design revolves around a six-node truss cell, forming the basis for a larger system. Actuation is a local feature of each such cell, providing local morphing throughout the structure. When constructing a foil using this method two types of cells with positive and negative in-plane Poisson's ratios are used for the pressure and suction side respectively. Strength calculations show that this wing construction weighs more than a conventional wing when allowable tip deflection under load is small. Weight should not cause the most concern in hydroturbine contexts, however. The



main concern for the design (from an aeronautical perspective) seems to be the actual foil skin, that needs to have large out-of-plane stiffness and at the same time be able to stretch to accommodate foil morphing. Ramrakhiani et al suggest several solutions, mostly involving several layers that interact to provide the desired skin characteristics.

Gandhi and Anusonti-Inthra [37] use a variable camber airfoil to demonstrate the desirable features of morphing skins. The approach used here integrates the skin as an essential part of adding stiffness to the foil. It is shown that unlike conventional airfoils, where the structural stiffness dominates the aerodynamic contribution in determining the displacement field, aerodynamic displacement may not be negligible. This depends on both the axial and flexural stiffness of the skin. A notable proposition in this paper is to integrate the actuators in the substructure in such a way that they contribute to the chordwise stiffness when not activated, but allowing smooth morphing when activated.

In *Active truss structures for wing morphing* [38], Baker et al describes a method that could minimize the actuation force requirements of a morphing camber wing. The Kagome lattice has the potential of becoming statically and kinematically determinant when properly manipulated. This provides a potential for a stress-free structure that withstands loading. By replacing some members of the lattice with linear actuators, it is ideally possible to achieve resistance-free deformation. Actual displacement calculations were performed by an iterative process including actuation forces on selected members of the truss structure and calculated nodal aerodynamic loads. The authors point out that there are some practical objections to the findings, perhaps the most important being the joint design. The design is dependent on pin joints, that do not transfer bending moments. An actual design will probably need to have joints using solid bonding, i.e. welded bonds. In further work by the same authors, such as in *The design of morphing aerofoils using compliant mechanisms* [39], methods for choosing the optimum placement of actuators is investigated. The results show that genetic algorithms are superior for small structures, while incremental forward stepping algorithms are as good and faster for large structures. It is also evident that there is a saturation point where the replacement of more passive members for actuators have little or no effect on the shape achieved. The same is observed for the maximum strain of the actuators. The algorithms are described further in *Determinate structures for wing camber control* [40].

Thill [35] mention several morphing concepts; One is the belt rib concept by Campanile et al [41, 42] where the ribs of an airfoil has been replaced by an increased number of rotatable spars, thus enabling camber changes across the span of the foil. The skin is essentially a belt surrounding the spars, hence the name. Another is the sliding rib concept by CRG [43, 44, 45] that uses a double set of ribs where one set slides on the other to increase the chord. In this design, a shape memory product called Veriflex®SMP was planned as skin material. Kudva [46] presents yet another approach to the substructure class, the *Eccentuator*. The Eccentuator is a basically a bent rod, thus a rotating movement at it's base is transferred to

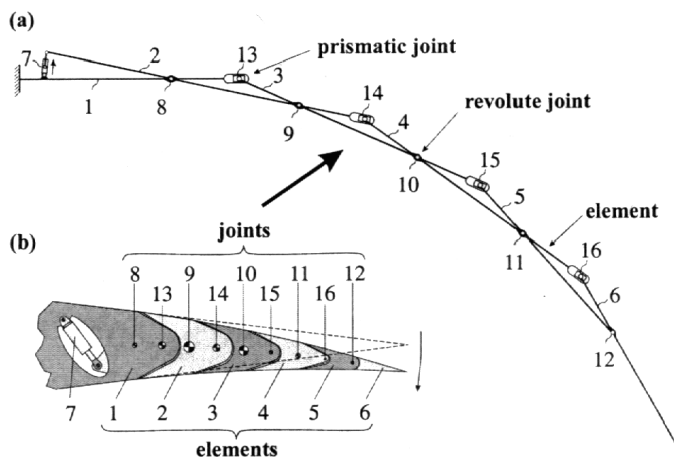


Figure 3.1: A schematic of Monner's 'finger concept', showing the principle of its actuation. Source: Monner [47]

transverse displacement at the tip. This forms the basis for a variable camber trailing edge that allows spanwise variation of camber. Monner [47] proposed a system dubbed the 'finger concept' by Thill. It is a variable camber concept that use a series of ribs connected in a similar fashion to the bones in human fingers. Thus morphing is achieved through the rotation of a series of joints. It is designed for mounting on the back of the wing ribs.

### 3.2.2 Morphing skins

By understanding the fundamental meaning of *morphing*; to change shape, it is apparent that the skin covering a morphing structure needs to be able to accommodate to area change. From chapter 3.2.1 it is deducible that a skin possibly will be required to transport load to a finite number of support points, i.e. the sub-structure joints supporting the skin. For this to be achievable, the skin needs to be flexible in it's plane, while retaining out-of-plane stiffness. When considering wear resistance one would have to compare to stainless steel in a hydropower context, or aluminium and graphite composites in aviation.

Kikuta [48] reports on the ability of different materials to act as skins on morphing structures. He has taken the aforementioned requirements in to account, and made a comparison of a selection of polyurethanes, copolyesters and woven materials. No materials are found to comply to all the requirements, though some have the potential. It is suggested that a combination of woven materials and polyurethanes could prove effective. The adolescence of this whole field is emphasized by the lack of standardized test procedures, and he suggests that some of the methods employed in his work could form a basis for such a standardization.

Thill [35] reports that skins from elastomers have good in-plane flexibility of up to 1000%, but limited ability to transfer loads to a substructure. Auxetic honeycombs are reported to offer a larger potential. An auxetic material is a material that expands when stretched, i.e. one that has a negative Poisson's ratio. The honeycomb is a structure that can be designed to have negative Poisson's ratio, as well as the more intuitive positive Poisson's ratio. It is possible to combine positive and negative Poisson's ratio materials in such a way that the resultant ratio is zero. That is a property of high value when expansion along a single axis is considered. It is believed that honeycomb or cellular structures, covered by a thin flexible skin, could serve well as a morphing skin.

Orthotropic structures have radically different stiffnesses in different direction. Such a characteristic is valuable to single dimension morphing, such as camber variations. Peel et al [49] demonstrates a method for making orthotropic fiber-reinforced skins from elastomers. Fibers are wound on to a mould, so all fibers are parallel. Thus the characteristics of the fibers only affect one direction, and stretching is possible normal to the fibers. Murray et al [50] suggest flexible matrix skins, that essentially have the same characteristics as Peel describe, as a solution for single dimension morphing, e.g. camber or span morphing. These materials are capable of handling out-of-plane loads when tensioned along the fibre/matrix axis.

A similar solution to the one mentioned above is the reinforced corrugated structure presented by Yokozeki et al [51]. Their skin consists of a loadbearing sublayer of corrugated CFRP<sup>1</sup> reinforced with CFRP rods, covered by a thin flexible film that provides a smooth surface. Stiffness is high in the rod direction, while flexibility is retained in the transverse direction.

Yokozeki et al [51] present a transition case towards multilayered skins. This was also suggested by Ramrakhyani et al [36], who proposed both a multilayered skin and a folded inner skin for their compliant mechanism. They suggest several layers of skin, not bonded to each other and thereby capable of large curvatures. The trade-off is reduced stiffness, and thus increased need for support. A support for the claim that unbonded skins are less stiff is presented by Gordon and Clark [52], who showed that removing the bonding from a multilayered beam reduced stiffness by one order of magnitude.

Ramrakhyani et al also suggested a segmented structure, similar to fish scales, as a possible skin solution. The individual scales move freely relative to it's neighbors in the skin plane, but interact to cause a much larger stiffness when subjected to loads out of the skin plane.

### 3.2.3 Continuous substructures

Madsen et al [53] have developed a controllable rubber trailing edge flap, for use on wind turbines. The goal is to reduce dynamic loads on the turbine in turbulent

---

<sup>1</sup>Carbon Fiber Reinforced Polymer

winds. The flap is made entirely out of rubber, and it's deflection is controlled by adjusting the pressure in reinforced voids inside it. Reductions of  $C_l$  by approximately 0,2 has been measured.

### 3.3 State-of-the-art

The literature studies suggest that state-of-the-art in morphing structures is the wing resulting from the MAW-project that was installed on an F-111 and made 59 flights in the 1985 to 1988 period, and the AAW-project that resulted in test flights with modified F/A-18 aircraft with new wing panels [35].

### 3.4 Possible hydroturbine application

The literature studies identified three important areas of secondary flow concern in Francis turbines; flow past stay and guide vanes and their impact on the runner, leakage flows past the guide vanes and swirl in the draft tube. The following section is a discussion of how morphing structures/skins are applicable in addressing these problems.

#### 3.4.1 Guide vane morphing

An ideal morphing guide vane minimizes it's wake and applies a local pressure distribution that counters the global pressure distribution (as described by Eide [2]), thus minimizing the strength of the rotor/stator interaction. One could of course add that it should approximate the ideal inlet angle  $\ast\alpha$  of the runner and retain it's control of the volume flow. From that perspective one would imagine that a fully morphable guide vane capable of cellular morphing (see e.g. [36]) would be the obvious choice. However, when replacing a part made of solid steel one has to raise the question of structural loads.

Antonsen [5] demonstrated that camber alters the pressure difference across guide vanes. The pressure differences affect the runner/stator interaction, along with the velocity deficiencies of the guide vane wakes. It is known from White [4] that flow direction is approximately parallel to the camber line at the trailing edge. Thus, cambering implies that a smaller angle of attack on the leading edge is required for a given flow deflection. Introduction of camber has a positive effect on both pressure distribution and runner inlet angle in the part load regime. The opposite is of course true for full load. At BEP the challenge is affecting pressure distribution without changing the inlet angle at the runner.

Even with extreme cambering, one can not easily imagine that the guide vane shaft can be eliminated. There is a need for actuation power to the foil, and the

wicket gate still needs to be closed. With that in mind either a morphing trailing edge or some form of varying foil thickness contrapment seems most promising. Morphing the guide vanes adds complexities to the turbine operation. Several camber morphing trailing edges were found in the literature study. Among these, the 'finger concept' [47] and the *Eccentuator* [46] seems the most promising. The 'fingers' that name this project are slender in the spanwise direction, allowing several to be stacked for the required strength. No variable thickness concepts were found. By reducing the thickness from the chord on one side, a camber can be achieved. CFD studies will be performed to assess the concept of camber morphing.

### 3.4.2 Leakage flow inhibition

The prerequisite for leakage flows in the clearance gap between guide vanes and turbine head covers is the pressure difference across the foil. Thus correct camber has the theoretical potential to inhibit leakages. However, it is not evident that the local pressure distribution can cancel the global pressure distribution along the entire foil, or that the required pressured distribution can be achieved without large losses due to heavy cambering. In the event of actuation power being transferred through the shaft, it is an option to use inflatable rubber seals to prevent leakage flows. That would allow the required clearance when the guide vanes are moved, and seal the gaps during stable operation.

### 3.4.3 Swirl flow inhibition

Kaplan turbines are able to pitch both guide vanes and runner blades, thus eliminating draft tube swirl. However, for heads higher than the Kaplan turbine is capable to handle, one still have to rely on the fixed runner alternatives. How tempting is not the thought of applying the same principles to e.g. Francis turbines? Note the major differences between the trailing edge of guide vanes and runner blades: where guide vanes are planar and of constant span, most Francis runner blades both twist and widen towards the outlet. Thus, material requirements are likely to differ, and morphing in a single plane is no longer sufficient. Introducing morphing structures in runners should be considered at least one step above cambering guide vanes on the hydro turbine evolutionary ladder.

### 3.4.4 Modes of operation

Because of the large dynamic forces at work in a turbine, active flow control would require very large actuation forces. It is therefore more applicable to introduce semi-active flow control. By this it is meant that the flow control mechanism is governed by main flow parameters, or turbine load parameters, rather than continuously responding to local instabilities. This sort of model predicted flow

control attempts to minimize adverse flow conditions rather than killing individual flow instabilities.

## Chapter 4

# Rig experiment

A rig demonstrating active flow control, using a computerbased input/output system, has been designed and constructed during this thesis work.

### 4.1 Introduction to the rig design

The rig consists of a steel pipe, installed vertically in the open flow channel at the NTNU Waterpower Laboratory, in which five holes of 60 mm diameter has been drilled at distances of 10 cm along the upstream side. The pipe encloses a rubber bellows, that protrude through the holes when pressurized by air. A pressure transducer is used to continuously monitor the bellows pressure and two valves control the inlet or release of air. The control interface is made in LabView, and has both an autocontrol mode and a mode for manual operation. During autocontrol operation, a velocity sensor monitors the freestream velocity of the flow. The velocity magnitude is used to decide if the rig is to go into an activated state where the bellows protrudes the holes, or revert to a neutral state where the bellows is flush with the pipe wall. The rubber protuberances are meant to reduce the von Kármán vortex shedding behind the pipe.

### 4.2 Design objectives

The objective of the experimental work has not been to try out or prove a morphing skin technology that is directly applicable in a hydro turbine, but rather to demonstrate active or model predicted control of a flow of water. For such a demonstration it is preferable to work with a time tested experiment that has relevance to the work of this report. For this reason it was decided to attempt model predicted control of the vortex shedding behind a cylinder. The control feature of the rig



Figure 4.1: An upstream view of the rig, with the velocity sensor on flow right.



should be able to identify conditions that cause vortex shedding, and implement some sort of response to attenuate the vortex shedding. The rig should also be able to measure if the response has had an effect. The following is an account of the experiment design process. Technical details are available in Appendix A

## 4.3 The rig design

### 4.3.1 The pipe

The experiment was to be set up in the open flow channel at the Waterpower Laboratory, NTNU. The channel connects two tanks, both with an adjustable overflow pipe, in the main water circuit of the laboratory. This makes adjustment of flow depth and velocity relatively easy. Because the channel walls are of steel, it has been decided to place the pipe vertically to allow e.g. LDV measurements to be performed (from top).

The cylinder with its actuator or response apparatus should be affordable and relatively easy to manufacture, in addition to having a 'morphing skin' feature. The literature study has shown that the size of the wake downstream, as well as the vortex-induced vibrations, is a concern in turbine rotor/stator interaction. It would be interesting if the rig assembly could reduce wake size and vortex shedding intensity, even though the experiment in itself is not primarily meant for further development. For this purpose the design by Owen and Bearman [23] has been of most inspiration. They added bumps to a cylinder, in this experiment an attempt is made to produce a 'morphing bump' by pressurizing rubber tubing in a perforated steel pipe.

The cylinder is made from a section of 0.1 m diameter stainless steel pipe. A series of five holes is drilled along the leading edge of the pipe. It is mounted in the flow channel; to the bottom by a rubber foot, and to the top of the sides by a stiff beam. The top mount is rigid enough to allow a solid fastening of the rubber foot by extending a threaded rod. Both ends of the pipe are closed, to prevent the rubber lining from expanding through other openings than intended.

### 4.3.2 The pressurized rubber bellows

Bumps of varying sizes is produced by adjusting air pressure in the rubber bellows, which is made from a motorcycle tyre inner tube. The tube was cut to length and the ends sealed, creating a slightly curved bellows. This is not the ideal shape, but it is an affordable and easily replacable solution. The bellows is then inserted in to the perforated steel pipe. Pressurised air is supplied through the valve mount, as one would normally inflate the tyre, but the check valve has been removed. The bumps grow or shrink proportionally to the pressure inside, but it is expected that at some critical pressure the rubber will either permanently deform or the tube will

burst. Testing to the maximum pressure utilized for this experiment has caused neither permanent deformation nor bursting.

Compressed air is supplied from the in-lab system and the inlet pressure is taken down to a level that takes both pressure impulses and lining strength into account. The pressurisation is governed by two electronically controlled 'binary' valves and a pressure transducer. One valve let in air, and the other releases it. The pressure transducer measures lining pressure, thus allowing change between pressure levels and modes of operation. The size of the bumps change with changing pressure.

### 4.3.3 Velocity measurement

Due to the large cross section of the channel, fluid velocity is relatively small; 0.2 to 1 m/s was expected in this project. This is relatively low for a pitot probe, as the pressure difference at 0.2 m/s is only 20 Pa. This constitute a 2 mm watercolumn. In an earlier work, the author did measurements in the channel with a Sensa RC2, which is an inductive device. The RC2 has a range of  $\pm 8$  m/s and an error of 3% for fluid velocities of 0.2 m/s. The device is a rather intrusive one, and must be positioned accordingly. The wake behind the sensor should affect neither the flow around the pipe nor the wake measurements. This is solved by placing the sensor to the side of the pipe, halfway between it and the wall. This should hopefully leave both pipe and wake sensor outside the probe wake.

### 4.3.4 Vortex measurement

From theory it is expected that the von Kármán shedding frequency will be no more than 5 Hz for the velocities that are expected to be achievable during operation (see chapter 2.5). The frequency and intensity of the oscillations are measured by strain gages mounted on a flat metal rod approximately 700 mm long. It is placed downstream of the pipe. Lengthwise the rod is placed parallel to the pipe. The flat side is parallel to the flow, thus subject to forces from the vortex velocity components that are perpendicular to it. The sideway deflection caused by the vortices is measured by two strain gages, that are built into a Wheatstone bridge with two resistors. The signal is logged; Fourier and peak-to-peak analysis indicates if there is any effect from the activated mode or not.

### 4.3.5 Control interface

LabView is used to create a program that acquires data from the Sensa RC2 and the pressure transducer, and controls the opening or closing of the valves. The PID control built into LabView was dismissed because the valves are 'binary', i.e. they are either completely open or closed. Given the learning purpose of this thesis, the author considered the option of designing the governor himself more profitable. The

governor is based on a virtual critical vortex shedding frequency, which according to equation 2.5 can be linked to freestream velocity, and set pressure levels to be attained in the rubber bellows at activated and neutral states. If the measured freestream velocity exceeds the critical value the governor will increase the pressure in the bellows to the activated pressure setpoint, correspondingly a freestream velocity smaller than the critical value will cause the governor to reduce the pressure to the neutral setpoint. Tolerances of a certain pressure deviation from the setpoints prevent continuous alternations between increasing and decreasing pressure during operation. In the event of a known critical frequency, e.g. a resonance frequency, this system could of course be extended to go into the activated state in a velocity band rather than above a certain velocity.

The control interface is also supplied with a manual mode, allowing manual inlet and release of air in the bellows. This feature has been used to determine the pressure levels for the activated and neutral setpoints, and during flow control concept tests. The manual mode is also practical for emptying the bellows before shutdown.

All activity is logged during a run. Date, time to one thousandth of second, measured values of pressure and freestream velocity, as well as the valve operation signal and the setpoints of pressure and frequency is logged to a .txt-file for later reference.

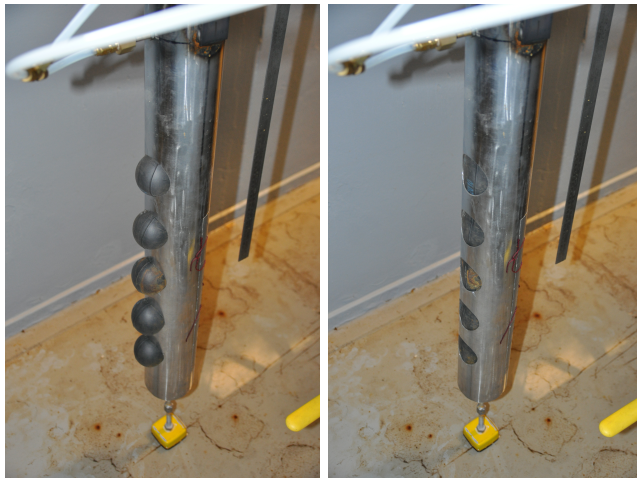


Figure 4.2: Left: The rig in activated mode, with the rubber bumps protruding from the holes. Right: The rubber bellows is flush with the pipe wall when the rig is in neutral mode.

### 4.3.6 The governor

There are three dynamic parameters in the governor; the freestream velocity  $U$ , the bellows pressure  $p$  and the mode of the previous cycle. Additionally some static parameters are set; activated mode pressure setpoint  $p_a$ , neutral mode pressure setpoint  $p_p$ , pressure deviation tolerance, critical velocity  $U_{crit}$  and velocity deviation tolerance  $U_{tol}$ . The parameter that describes the mode is in a feedback loop, providing info to the next cycle of the control sequence. The loop is run every 10 ms.

To determine whether the mode is to be activated or neutral during the present cycle, the freestream velocity measured is compared to  $U_{crit} \pm U_{tol}$ . If the last cycle was in activated mode  $U_{tol}$  is subtracted from  $U_{crit}$ , and if the last cycle was in neutral mode it is added. This provides a buffer against constant oscillations between modes when  $U$  is close to  $U_{crit}$ .

When the mode of the cycle has been set, the measured pressure is compared to the relevant setpoint value. If the pressure is not within the limits set by the pressure deviation tolerance, air is let in or released according to requirement by sending a signal to the appropriate valve.

### 4.3.7 Troubleshooting

The valve/transducer assembly was originally a compact construction, connected to the rubber bellows by an approximately 1 m long tube. Id est, the transducer was mounted very close to the valves, sources of pressures much higher or much lower than the bellows pressure, and relatively far from the bellows it was supposed to monitor. As a result the valves caused large pressure impulses on the transducer, limiting it's ability to produce good measurements of the bellows pressure during valve operation. In fact, these pressure pulses caused the governor to be useless. The pressure pulses caused the opening of one valve to trigger opening of the other valve. It was decided to move the pressure transducer and implement some physical damping to eliminate the problems. The transducer was moved to the bellows inlet, and connected to a T-joint by a length of tubing. A ball valve was installed on the tube and a piece of cotton twist was inserted into the tube as well. Choking the ball valve almost to the point of closing it entirely, and the cotton twist, proved effective during inlet of air. To reduce the pressure dips associated with release of air a long and narrow tube was mounted on the outlet. With these in place, and after locating and sealing a few minor leaks, the governor is capable of maintaining a set pressure with a tolerance of 5 kPa(gauge). The tolerance is small enough for bump size variation to be insignificant.

In order to further disturb the vortex sheet formation the pressure inside the lining was initially planned to be varied at a frequency equal to the expected shedding frequency. By consecutively opening and closing the valves, bump oscillation was meant to be achieved, but due to a relatively large pressurized volume compared to

the flow rate the filling and emptying time proved to be too large to achieve such oscillations.

Originally, the holes were drilled at 40 mm diameter. In the initial flow control concept tests with this configuration there was no measureable effect from the perturbations on the flow. It was decided to expand the holes to a diameter of 60 mm. During the same tests the velocity measurement proved more unstable than expected, prompting experimental re-placement of the velocity probe further upstream, to a position requiring more work to fix it in.

## 4.4 Rig operation

The flow is provided by the main pumps. They lift water to the inlet reservoir of the open channel on the laboratory loft, where it flows through the channel to the outlet reservoir and return to the pump reservoir through the weir pipe. The flow depth is controlled by adjusting the height of the weir pipe.

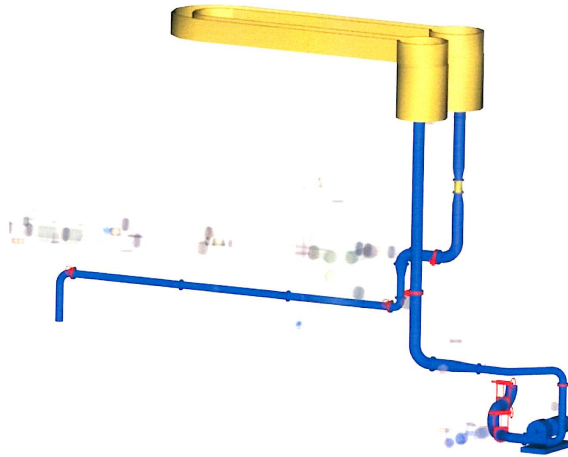


Figure 4.3: The configuration of the lab used when running the rig. The rig is mounted just before the bend in the open channel (yellow).

The rig itself does not require any fancy start-up procedure, but the velocity sensor should not be switched on before it is submerged. The author has made it a habit to pressurize the bellow to something close to the neutral set-point pressure before the cylinder is submerged. This is to avoid any complications from the bellow trying to displace water from within the cylinder walls. All this is done with the control software set to manual mode, once all is set the automatic governor mode can be switched on by the click of a button.

## 4.5 Rig test measurements

The purpose of the rig is not a purely scientific study of the effect of protuberances on the von Kármán vortex shedding, but rather to demonstrate it as a semi-active control method with the aim of suppressing vortex shedding. Thus, the main objective of this study is the active flow control. Nevertheless it was imperative to run a series of tests to verify if the desired effect is present, prior to further tests. These initial tests were done simply by comparing the vortex measurement data at activated and neutral cylinder modes.

### 4.5.1 First test measurements

A series of tests were run to verify the flow control concept as soon as the rig was thought to be fully operational. At this point the holes through which the rubber bellows protruded had a diameter of 40 mm. The test runs were executed at 30 r/min intervals of pump speed from 550 r/min to 670 r/min, consecutively in active and neutral mode.

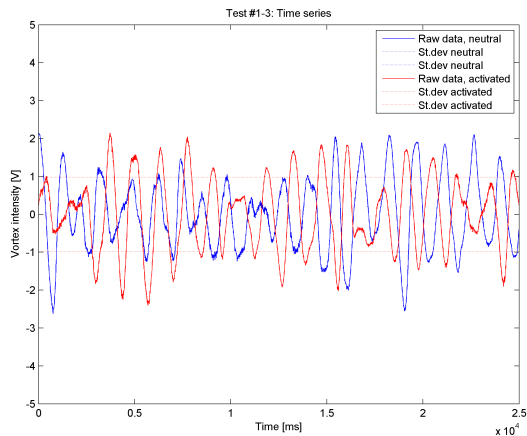


Figure 4.4: Time series of the 3rd run of the first measurement session.

Test run 3, presented in figure 4.4, shows no effect of the perturbations. The standard deviation of the voltage signal is the same in both activated and neutral mode. Thus it can be concluded that the perturbations did not suppress vortex shedding during this run. The FFT analysis suggest that the shedding is slightly more organized in the activated mode, as there is a more distinct frequency peak (with fewer sub peaks) can be seen here. Note that an amplitude modulation with a period of more than 10 s is present. It's origin is not immediately apparent.

Presented in figure 4.5 is test run 4, which exhibit a 38.5% reduction in wake

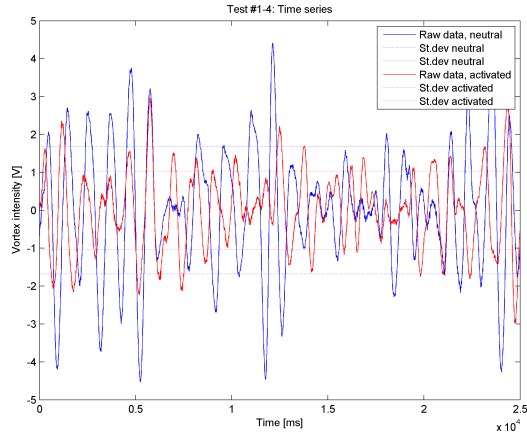


Figure 4.5: Time series of the 4th run of the first measurement session.

intensity when the mode is switched from neutral to activated. Thus, the concept appears to work fine during this run. The FFT analysis show that also here, the neutral mode has a relatively broad band of frequencies at which it oscillates, while the activated mode is a bit narrower. The amplitude modulation is visible during this run too.

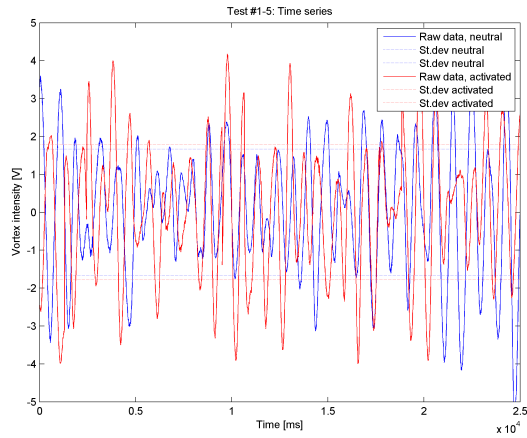


Figure 4.6: Time series of the 5th run of the first measurement session.

In test run 5 switching to the activated mode actually increased the size of the wakes, see figure 4.6. The same modulations as seen before are apparent here as well.

Key parameters are presented for all test runs in table 4.1. It can be seen that the three cases not presented graphically exhibit a modest change of vortex intensity (St.Dev) on the switch to activated mode; two of them with a reduction of 15% and 16.7%, and one with an increase of 4.3%. The velocity measurement device is set to average its measurement for 2 s between each sample is sent to the computer. The velocities presented in the table are mean values of these measurements. The velocity measurements show that the measurement set up or device is not very reliable. This is unexpected, because previous experience with the device suggests it should be ideal for the purpose. FFT analysis of the measurements suggest that the Strouhal number  $St$  is between 0.2 and 0.3.

Timeseries and FFT plots for all test runs are presented in the appendix, chapter B.1.

When analysing the results, a conclusion was reached that there was no effective flow control present. This spurred a quick return to the drawing board, and it was decided that the holes should be expanded to a 60 mm diameter.

Test #	Mode	Pump speed [rpm]	$U$ [m/s]	$\frac{A_a}{A_n}$ [-]
Test1-1	Activated	550	0.480	0.8454
	Neutral	550	0.176	
Test1-2	Activated	580	0.103	1.0433
	Neutral	580	0.182	
Test1-3	Activated	610	0.261	0.9961
	Neutral	610	0.285	
Test1-4	Activated	640	0.301	0.6147
	Neutral	640	0.334	
Test1-5	Activated	670	0.479	1.0691
	Neutral	670	0.489	
Test1-6	Activated	550	0.197	0.8322
	Neutral	550	0.205	

Table 4.1: Flow control concept test #1 - Results overview

## 4.5.2 Second test measurements

After expanding the holes in the cylinder to a diameter of 60 mm, a second concept test was run. Tests were done on the same pump loads as Test #1, to ensure roughly the same flow velocities. Additionally the velocity probe was moved upstream, on the assumption that the wake affected the velocity measurements. The averaging period of the probe terminal box was set to 2 s. The measurement runs were executed at 30 r/min intervals of pump speed from 550 r/min to 700 r/min, consecutively in activated and neutral mode.



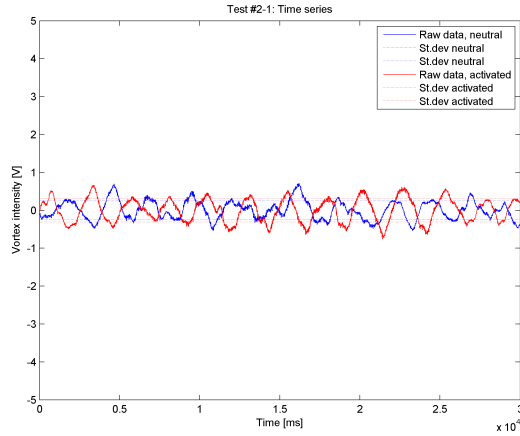


Figure 4.7: Time series of the 1st run of the second measurement session.

The first run of the second session, Test 2-1, is presented in figure 4.7. It is presented because it is the only run during this session in which the activated mode caused an increase to vortex intensity. Note however that the amplitude is very small, and that the sinusoidal appearance that can be recognised in the other plots is less pronounced. One should consider if this is because the flow is too slow for vortices to form properly in the cylinder wake.

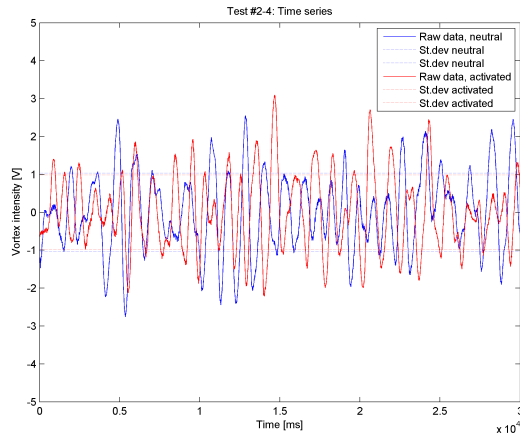


Figure 4.8: Time series of the 4th run of the second measurement session.

The vortex intensity is reduced by 4.5% in Test 2-4, representing the smallest reduction of the remaining cases. The amplitude modulation observed in the first tests are present here as well. It would appear that the modulation frequency is re-

duced in activated mode, however the low number of modulation periods measured is hard to draw any conclusions from.

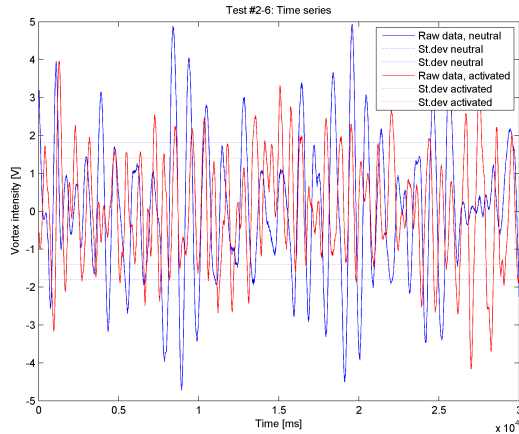


Figure 4.9: Time series of the 6th run of the second measurement session.

Test 2-6 is a good representative of the remaining four test runs of the second testing session. During these runs, the vortex intensity in activated mode was reduced by between 22.7% and 25.5% with respect to the intensity at neutral mode. In all these runs, the amplitude modulations at activated mode becomes more chaotic compared to the neutral mode modulations.

The key parameters are presented in table 4.2. Ideally, the measured velocities should be similar to the first test session, but the measurements were taken at another point in the flow during the second session, so some difference is to be expected. However, many of the velocity means during this session suggest that the velocity measurements are quite a bit off.

Timeseries and FFT plots for all test runs are presented in the appendix, chapter B.1.

### 4.5.3 Discussion: Rig test results

The studies show clear indications of regularly shed vortices from the cylinder. This is as expected. The first test series exhibited contradictive results with respect to the flow control concept. There were some promising single runs, but no conclusive reduction of vortex intensity. Thus an overall failure of the flow control concept was the result of the first test session. On the assumption that the wave steepness was insufficient the hole diameter was increased. In the following test session all but

Test #	Mode	Pump speed [rpm]	$U$ [m/s]	$\frac{A_a}{A_n}$ [-]
Test1-1	Activated	550	0.130	1.2432
	Neutral	550	0.083	
Test1-2	Activated	580	0.245	0.7570
	Neutral	580	-0.003	
Test1-3	Activated	610	0.358	0.7557
	Neutral	610	0.288	
Test1-4	Activated	640	0.295	0.9554
	Neutral	640	0.634	
Test1-5	Activated	670	0.092	0.7447
	Neutral	670	0.470	
Test1-6	Activated	700	0.413	0.7735
	Neutral	700	0.325	

Table 4.2: Flow control concept test #2 - Results overview

the first test run showed a clear reduction of vortex intensity. Thus it was proved that the flow control design is capable of reducing vortex intensity. For reference the results are compared to those reported by Owen and Bearman(O&B) [22, 23].

Because the perturbations of the present studies have a semi-spherical shape, the hole size is an excellent perturbation height scale. Using this definition, the investigated height to length ratios are  $h/\lambda = 0.4$  and  $h/\lambda = 0.6$ , well within the vortex free region of O&B's studies. The Reynolds number of the test runs has been in the range of 2000 to 5000. This is within the range of Reynolds numbers in the studies by O&B that were performed in water. They used bumps of up to  $0.5d$  height, but spaced them wider than in the present study. They found that the bumps reduce body oscillation (as a response to vortex formation) to zero when the damping parameter  $m^*\zeta$  is larger than 1.5. Here  $\zeta$  is the damping ratio and  $m^* = \frac{m_{sys}}{m_d}$  is the ratio of body mass to the mass it displaces. However, in the present studies  $m^*\zeta$  is small because water is displaced mainly by air, thus body oscillations are not expected to be entirely suppressed. One can argue that for sufficiently large damping parameter values the vortices are no longer able to excite oscillations in the body, even though some vortex shedding is present. The study of this thesis does not measure the body oscillation, but rather the oscillatory variation of flow direction in its wake. O&B report a body oscillation amplitude reduction of 25% for cylinders with bumps. Similar reductions of vortex intensity was found in the present study. There appears to be conjunction between results of the two studies.

For a constant damping parameter value a close to linear relation between body oscillation amplitudes and vortex intensity might be plausible, since the measurements of this thesis denominate the transversal force on the vortex sensor as vortex intensity. By this assumption, there is good correlation between the present results and those of O&B. The main difference between the two is the distance between bumps and the unidirectional character of the present rig arrangement. It should also be noted that the shape of the perturbations are slightly different, with a less

semi-spherical appearance in O&B's experiments. It is concluded that the flow control concept is valid, the cylinder has the physical potential of doing its job. It should be remarked that the velocity measurements during the concept test sessions did not have a sufficiently high quality for good automatic governor operation.

With respect to the velocity measurement quality, velocity measurements as a governor trigger was chosen due to the upstream nature of the measurement. Upstream is a term that in this sense may be used both literally for the actual position of the probe, and metaphorically to describe our opportunity to predict vortex shedding frequency and intensity if the velocity is known. In fact the velocity measurement is, at least hypothetically, used to calculate the very same property that the vortex sensor measures. So why not simply monitor the vortex intensity in the wake, or even the cylinder oscillations? This is answered most easily by quoting Owen and Bearman; ...*The transverse oscillations of the cylinder with bumps developed extremely slowly compared to the plain cylinder...*[23]. An upstream measurement renders it possible to predict adverse conditions, and activate the flow control device before the adverse effect builds up to its undesired maximum. Thus, a proper velocity measurement can be used to predict oscillations, knowledge which in turn can be used to slow down and dampen transients. Of course, in an arbitrary application the actual measurement can be substituted for another, more practically achievable, measurement with a measurand that is coupled to velocity. E.g in civil engineering a pressure sensor at the bottom of a canal can provide information about flow depth, which can be correlated to flow rate and velocity.

## 4.6 Autocontrol mode tests

The primary test scheme for the autonomous mode is based on leaving the governor in autonomous mode, while varying the flow. Practically, this is a test of the velocity measurement quality, as well as an illustration of the flow stability. Because of the previously unstable velocity measurements, the velocity meter was set to average measurements for 5 s. Thus, the response time could be up to 5 seconds. The entire test period is presented graphically in figure 4.10. The second concept test, chapter 4.5.2, is considered proof of concept, thus effort to determine vortex intensity damping has not been spent here. The activated mode pressure setpoint is 220 kPa and the neutral is 50 kPa. The critical velocity setpoint is set to 0.3 m/s with a tolerance of 0.03 m/s. Vortex intensity is plotted as percentage of the total mean value of the vortex measurement.

The flow rate was increased at a random rate, before it was reduced again. The first activated mode interval in figure 4.10 is a result of faulty measurements. From 70 s to 350 s the velocity measurements were reasonable, with the exception of the two dips to zero. As it can be seen, some time after a mode change the governor works the valves to stabilize the pressure. This is a trade-off from the physical damping, the alternative would be continuous valve activity.

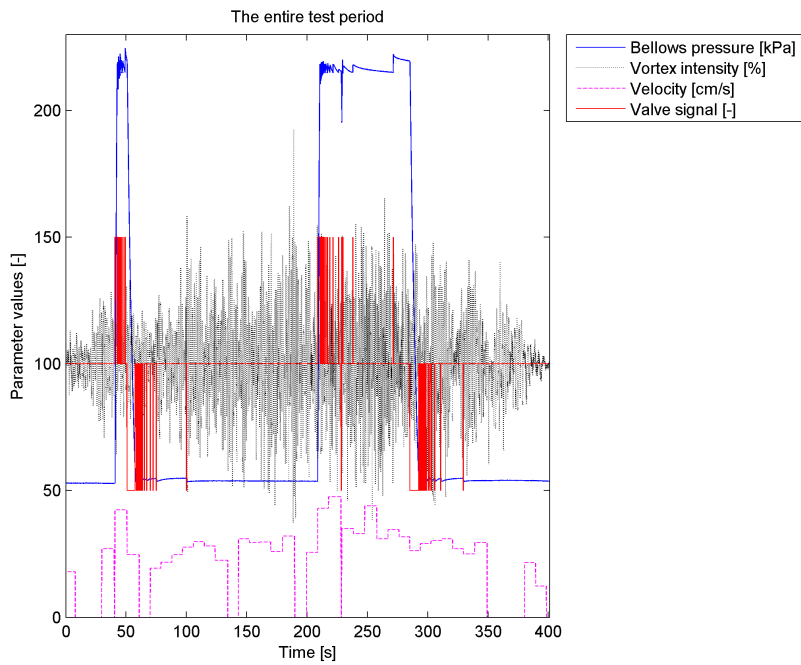


Figure 4.10: The entire test run with the rig set to autocontrol mode. The value of the valve signal signify valve opening; 50: release of air from bellows, 100: both valves are closed, 150: inlet of air to the bellows.

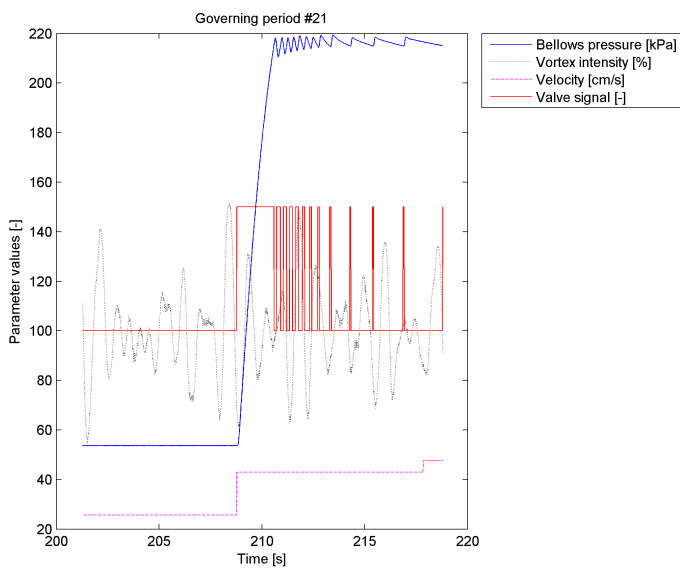


Figure 4.11: An example of the response as the measured velocity increase to exceed the critical value.

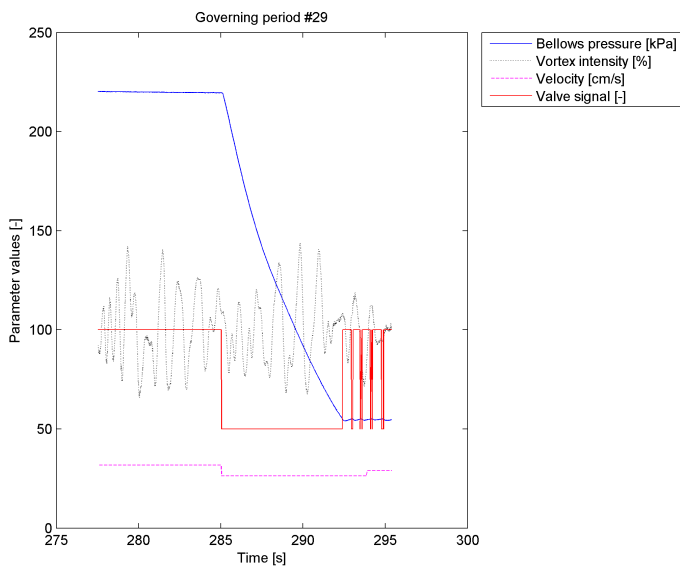


Figure 4.12: An example of the response as the measured velocity decrease to a level below the critical value.

Figure 4.11 show the response to an increase of velocity causing the critical velocity limit to be exceeded. The governor respond by opening the inlet valve, and the bumps are inflated. As the pressure reach the activated pressure setpoint the valve is closed, because of damping effects the pressure has not yet stabilised, and the works the valve for some time to stabilise the pressure. As is apparent from the figure, the period between each valve opening increase, until it nearly cease. Further on, when the flow is decreasing, the measured velocity again is reduced to less than the critical velocity, and the rig revert to it's neutral state by opening the release valve. As can be seen in figure 4.12, a process similar to the one described above takes place in order to stabilise the bellows pressure at the neutral pressure setpoint.

The autocontrol test showed that again it is the quality of the velocity measurements that compromise the governor performance. A better velocity measurement solution should be implemented here. The calibration report for the differential pressure transducer used to monitor the bellows pressure report a max uncertainty of 37 Pa, indicating that the dismissal of a pitot tube as velocity probe was not wrong given the circumstances. The recent experiences with the Sensa RC2 indicate that the use of a pitot probe could have been investigated better. The calibration report is available in appendix A.





# Chapter 5

## CFD

CFD (Computational Fluid Dynamics) tools are powerful aids in fluid dynamics. An important part of this thesis work is the assessment of a morphing concept by use of CFD. For this purpose, the ANSYS 13 package was put to use.

The simulations aim to discover if there is cause for further investigations into the construction of morphing guide vanes. A series of test cases, involving several camber configurations for a single angle of attack, are simulated, in order to see the effect of guide vane camber on runner torque variations. This is in many ways a variation of the CRTEF [53], but the application is quite different. Morphing guide vanes will be the sole method of implementation if it is proven that changing the camber can decrease torque fluctuations or increase efficiency.

### 5.1 Governing equations and models

The base equations of fluid flow are the Navier-Stokes equations [4], which describe continuity, momentum and energy conservation. A unique solution has not been found for viscous flows. This has led to the development of numerical methods that replace parts of the physical equations with models, e.g. turbulence modelling. This is the concept of all CFD programs that do not do direct numerical simulations.

Two important turbulence models are the  $k - \omega$  and the  $k - \epsilon$  models. The  $k - \omega$  model is best suited for modeling turbulence in boundary layers, while the  $k - \epsilon$  has proven successful in freestream flow. Thus the two models both have qualities sought after when modeling turbines. To meet the requirements of modeling flows that have both freestream and boundary layer domains, Menter [54] developed the shear stress transport model (SST). It blends the  $k - \epsilon$  and the  $k - \omega$  models in such a way that it equals to the  $k - \epsilon$  model in the freestream, and the  $k - \omega$  model in the boundary layer.

## 5.2 Simulations

Simulations of cambered guide vanes in a Francis turbine has been run, to investigate the impact of camber morphing on the rotor/stator interaction. Geometry from an early version of the Cahua runner was obtained, and a script was written to generate different guide vane foil shapes. The input parameters for the design of the foil are foil length, relative thickness, camber, point of maximum camber and angle of attack ( $\alpha$  in figure 2.3), but the parameter study only involves changes of camber and angle of attack. In general, positive and negative camber of up to 2% of foil length is used, in addition to a reference case of zero camber.

All simulation work has been within the ANSYS Workbench environment. Turbo-grid cells were set up for stay vanes and the runner with cone attached, in addition to a separate cell for each guide vane blade. A separate CFX cell is set up for each case, connected to the runner and stay vane meshes, and one of the guide vane meshes. Upon addition of new CFX Post features, a new solution cell is connected to each CFX cell, after set up and subsequent duplications.

Each simulation is a compilation of the stay vane mesh, a case specific guide vane mesh, and the runner with cone mesh. These are assembled to four domains; stay vanes, guide vanes, runner and cone, and connected using domain interfaces in CFX Pre. For continuity purposes there is the same number of stay vanes, guide vanes and runner blades. Only a section of the turbine is simulated, and having the same number of all blades has proven to minimize interface problems. The turbine is 'made complete' by using periodic interfaces on the azimuthal boundaries. The reference pressure is set to 1.01325 bar. The inlet is a pressure inlet across which the total pressure has been set to be 22.5 bar, additionally the velocity components has been set in accordance with the given best efficiency point flow angle, with no axial velocity component. The runner rotates at 650 r/min. The outlet has a relative pressure of  $-0.5$  bar. All walls are smooth, no slip walls.

The simulations are set up using two consecutive configurations, with the completion of a steady state solution triggering, and providing initial conditions for, a transient simulation. During the steady state simulation the domain interactions are of the 'Frozen rotor' type, while the 'Transient Rotor-Stator Interface' is used during transient simulations. The convergence condition for the steady state simulations is residuals with RMS value of less than 0.0001. The transient simulations are set to run 110 timesteps, each at 0.0000641 s, which corresponds to a rotation of  $0.25^\circ$  per timestep. Transient results are stored every fifth timestep. With this timestep size, it takes 84.7 timesteps for the runner to rotate through one blade pass sequence. The additional timesteps allow for some run-in of the simulation during the first timesteps.

### 5.2.1 Meshing

ATM; Automatic Topology and Meshing, is the default meshing method in ANSYS Turbogrid [55]. It produces meshes of quite high quality, even if it can't compete with expert grid refinement. The method is based on the creation of a master topology, to which the grid is bound. The shape of the topology is unchanged, though scaled, between each case. This allows refinement to be performed in critical topology sectors, such as around leading and trailing edges. The topology is also ideal for scaling and parameter studies. See an example of the grid in figure 5.1

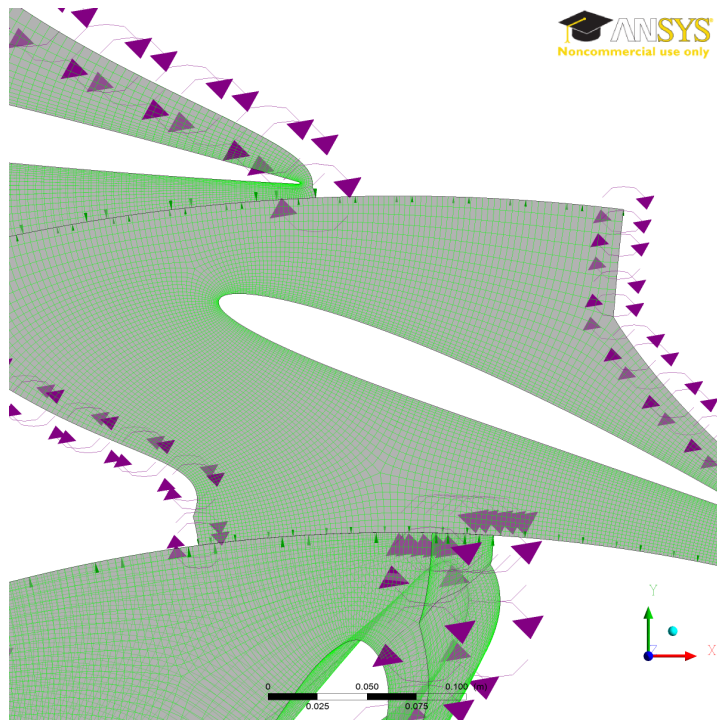


Figure 5.1: Example of the guide vane mesh, NACA2509 at  $22^\circ$  angle of attack.

The same ATM grid was generated for all cases simulated, by first creating one grid that was subsequently copied before new guide vane profiles were introduced. It should be stressed that the grids are not equal, and the node count changes from case to case due to changes in camber and angle of attack. Nevertheless, the general layout of the mesh remains the same for all cases.

The full mesh assembly (illustrated in figure 5.2) has up to about one million nodes, with the cases of small angle of attack having around 200000 fewer nodes than the largest. This is the upper limit that memory on the available computer allows. A little less than half the nodes are located in the guide vane mesh, with the cone

and stay vanes being the coarsest sections.

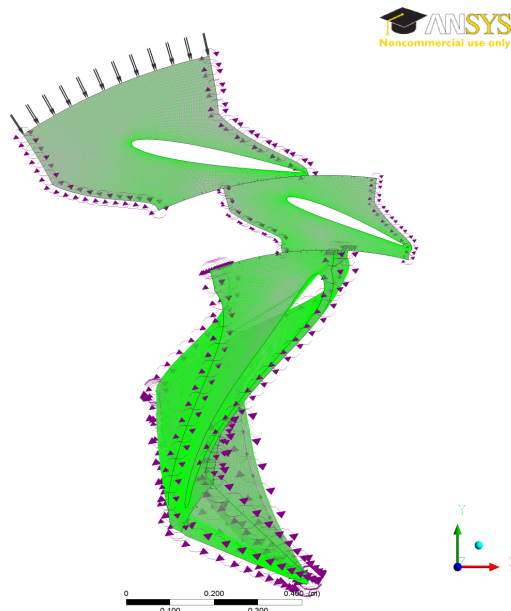


Figure 5.2: Overview of the assembly of the stay vane, guide vane and runner meshes.

## 5.2.2 Case overview

Camber is varied for a variety of inlet angles, that is to say guidevane angles of attack. The BEP inlet angle is given as  $23.579^\circ$ . Table 5.1 gives an overview of the cases that was investigated.

## 5.3 Expected simulation results

The torque variation is, as shown in chapter 2.4.1, caused by velocity and pressure wakes from the guide vanes. The torque fluctuates as the blade travels through the wake. The runner is placed in such a way that its leading edge is outside the wake during the steady state simulation, and travels through it during the subsequent transient simulation. One should observe that the torque drops when the leading edge enters the wake. It is expected that the changing camber will affect the size of the wake. The important question is if the dip is smaller for a certain camber, which will be identified as the ideal camber for the given flow rate.

$\alpha$	NACAxxxx	$\alpha$	NACAxxxx
16°	-1509	23.579°	-1509
	0009		0009
	1509		1509
	2509		2509
18°	-1509	25°	-2509
	0009		-1509
	1509		0009
	2509		1509
20°	-1509	26°	-2509
	0009		-1509
	1509		0009
	2509		1509
22°	-1509		
	0009		
	1509		
	2509		

Table 5.1: An overview of the different NACA profiles and angles of attack investigated.

One should expect some change in flow rate when comparing cases with the same base angle of attack, since the total head is fixed. This inflicts some restrictions on the comparison of results. When evaluating the results one can not merely compare different cambers for the same base angle of attack, but need to consider the actual flow rate and head. One could expect, on part loads, that wakes are reduced, while simultaneously the flow rate is increased. Thus, cambering of the guide vanes should require reducing the angle of attack; the gain from introducing camber might be lost.



# Chapter 6

## CFD Results

### 6.1 Performance data

The performance calculations are based on the the transient simulations. Key data; Head  $H$ , mass flow rate  $\dot{m}$ , power  $P$  and efficiency  $\eta$ , is extracted from the transient simulation results and averaged over a blade pass period.  $g = 9.8 \text{ m/s}^2$  and  $\rho = 997 \text{ kg/m}^3$  are constants (in this context). See equations 6.1 through 6.3 for definitions used. The performance results are presented in table 6.1.

$$H = \frac{\Delta p_{tot}}{\rho g} = \frac{p_{tot@StayvaneInlet} - p_{tot@ConeOutlet}}{\rho g} \quad (6.1)$$

$$P = M_z \cdot \omega \quad (6.2)$$

$$\eta_h = \frac{P}{\rho g Q H} = \frac{\rho P}{\dot{m} p} \quad (6.3)$$

Figure 6.1 shows the results in graphical form. It can be seen that excepting the presumed outlier (NACA0009, AOA 23.579°), the best efficiency is achieved with the NACA2509 profile. Note that the difference in efficiency at part loads appear notably smaller when plotting against power output than angle of attack. This is due to significant differences in mass flow at the same base angle of attack for the different foil profiles. Thus, the NACA2509 foil gives a higher load than the NACA-1509 foil at the same base angle of attack, which might explain the higher efficiency. The turbine efficiency peak at more or less the same load for all foil shapes, at around 1.4 MW per blade. This is a good indication that the guide vane design might change the maximum efficiency for a particular runner design.

$\alpha$	NACAxxxx	Head [m]	Mass flow [kg/s]	Power [MW]	$\eta_h$
16.000°	-1509	231.291	440.786	0.885	0.885
	+0009	231.375	454.416	0.920	0.892
	+1509	231.493	468.806	0.957	0.899
	+2509	231.467	482.030	0.990	0.905
18.000°	-1509	232.426	504.399	1.037	0.902
	+0009	232.515	517.962	1.072	0.907
	+1509	232.735	531.684	1.109	0.913
	+2509	232.944	545.760	1.147	0.920
20.000°	-1509	233.376	566.001	1.190	0.918
	+0009	233.451	578.290	1.223	0.923
	+1509	233.393	590.759	1.256	0.929
	+2509	233.375	602.982	1.289	0.933
22.000°	-1509	233.209	621.151	1.321	0.930
	+0009	233.095	632.344	1.349	0.933
	+1509	232.887	642.998	1.375	0.936
	+2509	232.651	652.608	1.398	0.939
23.579°	-1509	232.427	660.453	1.403	0.932
	+0009	232.275	667.038	1.442	0.949
	+1509	231.765	679.006	1.443	0.935
	+2509	231.468	688.237	1.462	0.935
25.000°	-2509	231.540	684.107	1.441	0.927
	-1509	231.143	693.269	1.460	0.929
	+0009	230.756	701.696	1.477	0.930
	+1509	230.409	710.667	1.496	0.931
26.000°	-2509	230.467	706.991	1.479	0.926
	-1509	230.096	715.375	1.496	0.927
	+0009	229.730	723.778	1.513	0.928
	+1509	229.437	731.366	1.527	0.928

Table 6.1: An overview of the performance results

## 6.2 Torque variations

Axial torque  $M_z$  on the runner shaft is monitored during the transient simulations, providing information about the variation within a blade pass period. The data has been processed to find the maximum and minimum values of torque during the cycle. The results are plotted against the power output in figures 6.2 and 6.3. The torque (naturally) increase linearly with the power output, or rather it is the power output that increase linearly with the torque. The magnitude of torque variation, expressed as the peak to peak value, increase in a similar manner. It can also be seen that the magnitude of torque variation is considerably smaller for profiles of increasing camber. This corresponds to the findings on efficiency.



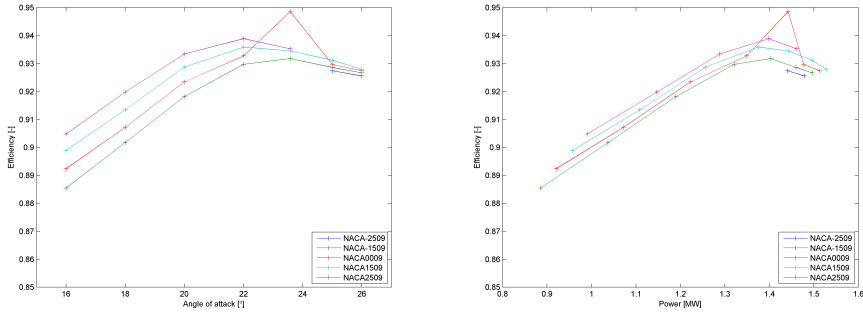


Figure 6.1: The efficiency  $\eta$  plotted against the angle of attack and power output for a turbine section.

### 6.3 Wake sizes

The guide vane wakes are extracted at 7 lines that has been constructed in the wake area of the guide vane domain. The lines are the same for all angles of attack and guide vane profiles. As a result, the actual flow direction is not perpendicular to the lines, but close to it. The lines are 85.6 mm long. The velocity profiles are key elements in determining if cambering has any effect on the wake size. Previous work (e.g. Antonsen [5]) suggest it, the present study should investigate if there is further to gain from morphing the guide vanes with respect to camber.

Ideally several guide vane shapes should be investigated at the same head and flow rate. However, comparing results at similar flow rates should allow a general trend to be found. Thus, comparing the velocity profiles, head and mass flow of the test cases can provide an estimate for an ideal camber model. In order to more easily compare the velocity profiles, they are normalized. Because the lines span some radial space there is a freestream velocity gradient along them, from the outermost to innermost point. A conditioning function has been worked out to remove the gradient from  $U$ . The function is such that the product of the function and the velocity at any point along the line would be constant if the velocity gradient was perfectly linear;

$$\begin{aligned}
 f_{conditioning} &= \left(f_1 - \frac{\Delta U}{\Delta y}\right) + \frac{\Delta U}{\Delta y} \cdot y \\
 \frac{\Delta U}{\Delta y} &= \frac{f_2 - f_1}{U_{end} - U_{start}} \\
 f_1 &= \frac{U_{mean}}{U_{start}} \\
 f_2 &= \frac{U_{mean}}{U_{end}}
 \end{aligned} \tag{6.4}$$

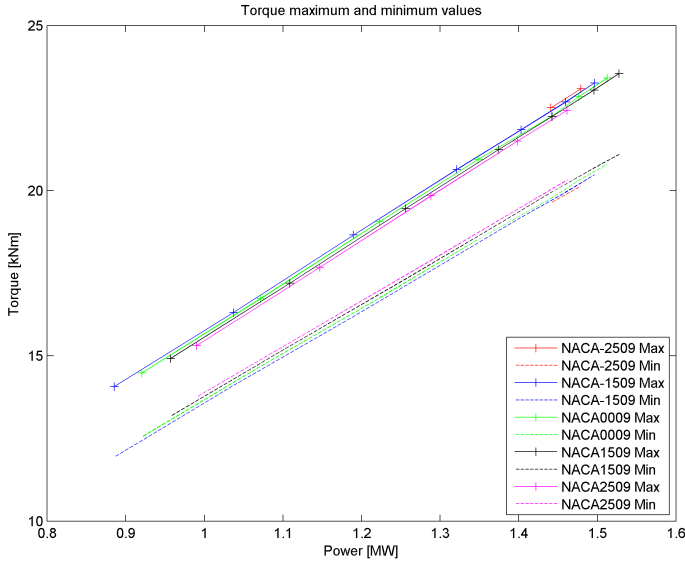


Figure 6.2: The maximum and minimum values of torque plotted against the power output of the runner.

The velocity  $U$  and position  $y$  is then normalized using the following equations.

$$\begin{aligned} u_n &= \frac{U-u(y)}{U} \cdot \sqrt{\frac{x_w}{L}} \\ y_n &= \frac{y}{\sqrt{x_w} \cdot L} \end{aligned} \quad (6.5)$$

As can be seen in figure 6.4 the wakes do not change significantly for the different profiles. There are some small differences though, and figure 6.5 show that the differences in wake widths are profile specific. Note that the widest wakes are those of the NACA2509 profile, the one which performed best with respect to efficiency and torque variations. Figure 6.6 show the viscous drag on the guide vanes, calculated from the wakes. There are generally very small magnitude differences between the foil shapes, but below best load there is distinct foil dependency. The viscous drag has been calculated and normalized by the following equations;

$$\frac{F_{D,Viscous}}{b} = \sum \rho u(U-u)\Delta y \quad (6.6)$$

$$C_d = \frac{F_D}{\frac{1}{2}\rho U^2 A} \quad (6.7)$$

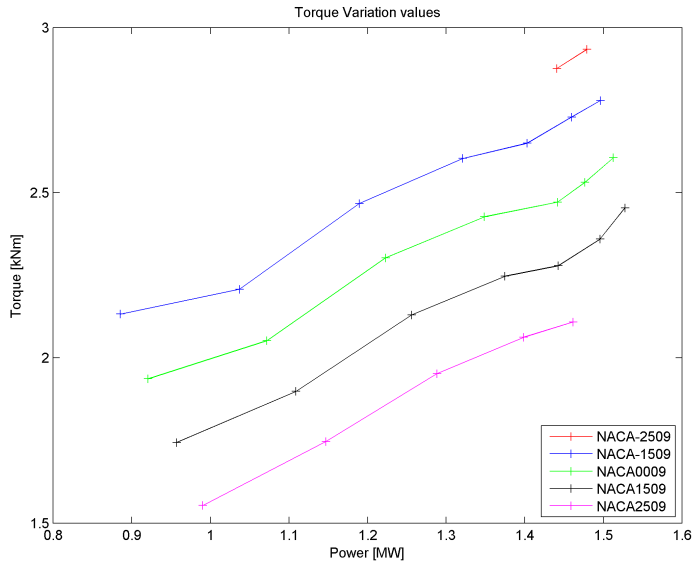


Figure 6.3: The peak-to-peak variation of torque on the runner during one blade pass period.

The flow distance  $x_w$  from guide vane trailing edge to runner changes significantly from full load to part load. By evaluating the velocity profile at the domain interface connecting the guide vane mesh to the runner mesh one can evaluate different wakes, 'as seen' by the runner. The most prominent disadvantage of this approach is perhaps that the domain boundary is not perpendicular to the flow. Obviously, information about the spanwise velocity distribution at the trailing edge is a more appropriate characterisation of the wake. However, for this case it is also of interest to know the flow conditions the runner is exposed to. The domain interface is at a constant position with respect to the runner blade and therefore independent of changing guide vane settings. This makes the boundary a good reference plane for additional knowledge. Because the flow does not move perpendicularly across the interface, the span of the wake does not all cross the interface at the same distance  $x_w$  from the trailing edge. For that reason, the velocity profile is asymmetric. On figure 6.7 it can be seen that one side (the left) change less than the other from case to case. The same side also exhibits a sharper velocity gradient.

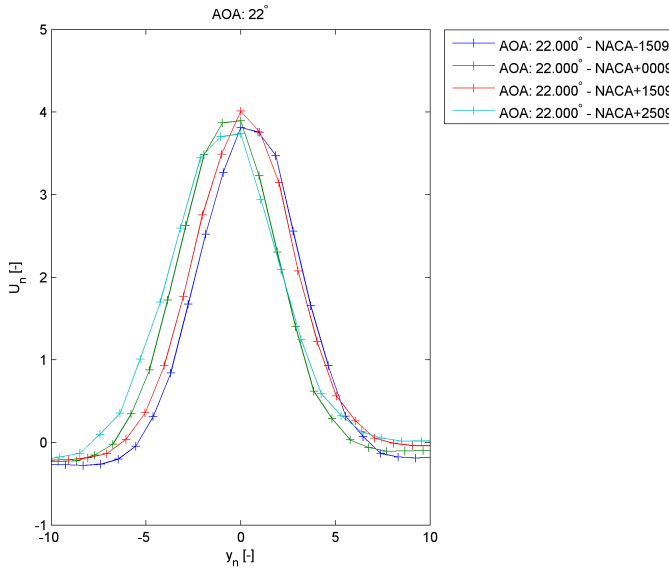


Figure 6.4: Wake velocity profiles at the center wakeline with  $22^\circ$  angle of attack. All cases are normalized.

## 6.4 Forces on the guide vane

The evaluation of surface pressure at a large series of points along the center line on the guide vanes form the basis for calculation of torques and forces on the blade. The data points have been collected during the steady state simulations. The main results are presented here. The main results include torque on the guide vane shaft, but the same data can readily be used to evaluate the torque experienced by an arbitrary joint in e.g. a foil of the 'finger concept' [35].

The torque on the guide vane shaft has been calculated in accordance with the simulations. All foil geometries in the simulations were calculated with a shaft axis placed at 30% of the chord length from the leading edge. The axis of torque in the torque calculations is the same. All bladeloading data has been projected to its proper foil geometry, to provide blade surface angle and surface section width for each bladeloading data point. The results are plotted against power in figure 6.8. With the exception of the smallest load, there are no significant differences in torque on the different NACA profiles, with respect to power output. As should be expected the torque is large at small angles of attack, when the foil is more at an angle to the flow. The effect of camber on lift is illustrated well when plotted against angle of attack in figure 6.10. The direction of lift has been defined as towards the runner shaft. It can be seen that the foils with a camber-induced lift in the negatively defined lift direction (the NACA1509 and NACA2509) reverse

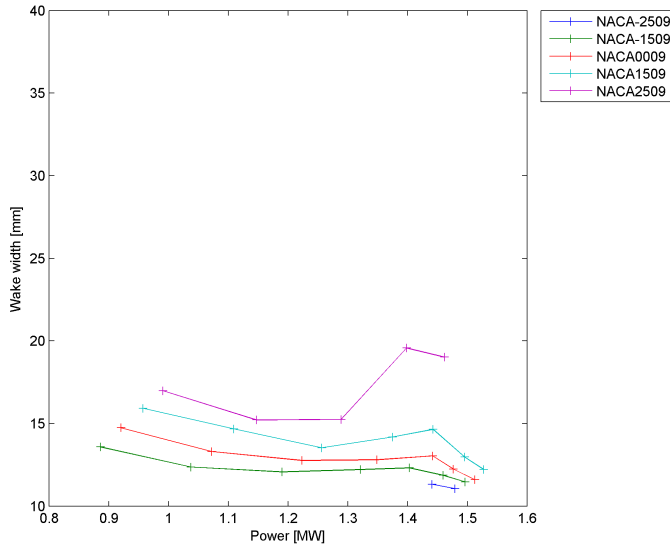


Figure 6.5: Wake widths sorted by guide vane shape and plotted against power output.

torque direction at smaller angles than the others.

The pressure drag of the guide vane is readily calculated from the same data source, by integrating the x-direction pressure components around the foil. The drag results are presented in their normalized state, as the drag coefficient  $C_d$  (see equation 6.7). The pressure data was collected along the center line on the guide vane, and is only valid there. Thus the  $C_d$  is on a per-length scale, since the 'projected area' is actually the foil thickness. Were one to estimate the pressure drag on the entire foil, care should be taken to take the spanwise variation of the pressure distribution into account. The results are presented in table 6.2, and represented graphically in figure 6.9. As seen in the figure, the drag on the different profiles change very differently with respect to power. At high loads the drag is of the same magnitude for all foils;  $C_d \approx 0.9$ . At the lower part loads there are large differences, with variations from  $C_d = 0.343$  to  $C_d = 0.991$ . There is an increasing trend towards constant drag as the degree of camber increase. With the NACA2509, which has already showed admirable performance, the drag remain stable when the turbine load increase. The calculated drag values are quite cluttered, making precise connections to other result trends hard.

The lift  $F_L$  on the guide vanes, displayed in figure 6.10, show much clearer trends than the drag. The lift coefficient  $C_l$  is defined by the same equation as  $C_d$ . As has already been mentioned in chapter 2.4.1, 'pressure wakes' behind the guide vanes affect the runner much like the velocity wakes do. It is apparent from the

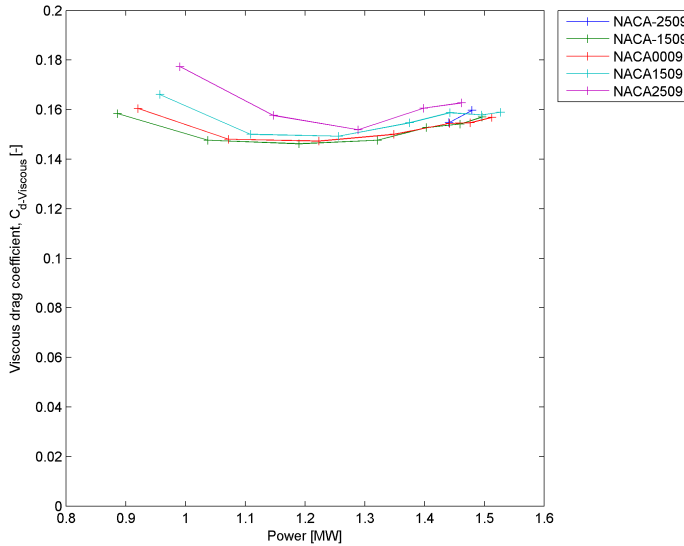


Figure 6.6: The viscous drag on the guide vane, sorted by NACA profile and plotted against power.

figure that the pressure difference across the foil is smaller on the NACA2509 foil. The difference between the largest and smallest lift coefficient at any given load is approximately 0.1 for a large part of the load range.

## 6.5 Discussion: CFD results

The hypothesis behind the simulation scheme stipulated that a series of continuously changing guide vanes would yield improved efficiency and reduced power fluctuations in the turbine operation range. This would be achieved, because at every angle of incidence there should be one foil shape that cause a smaller wake than any other. By this hypothesis a guide vane cambered to one extreme would perform best at one side of the range, while an oppositely cambered guide vane would perform best at the other side of the range. To exploit this, one would have to be able to continuously change the camber of the guide vanes; they would need to be morphed. The simulations modelled a turbine section with a mesh assembly where the guide vane mesh would be unique for each case. The produced results; a data array consisting of 28 data sets has been evaluated to determine the validity of the hypothesis.

The litmus test for the simulation results, apart from their successful convergence, is the performance data. Figure 6.1 looks very much like one should expect, with

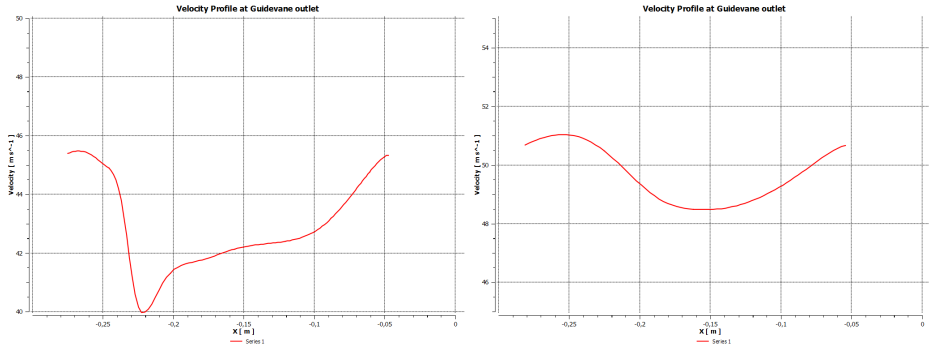


Figure 6.7: The wakes of two NACA0009 profiles at different angles of attack, taken at the guide vane to runner domain interface. Left: 25°, right: 16°. As can be seen, it is hard to take conclusions for one angle of attack to another, even if the foil geometry is the same.

a clear efficiency peak for all NACA profiles. Furthermore the peaks falls into a very narrow range of power output, indicating that the characteristics of the runner is caught by the simulation. The mass flow at the best efficiency point also correspond to the mass flow given as the rate load of the runner. This is important, because rather than setting mass flow and velocity components as inlet conditions, total pressure and velocity components were used. In essence this implies that the simulations catch the characteristics of the runner, and make good estimations of its performance. By this logic, there is a clear variation of overall turbine performance when different guide vane profiles are installed.

There is a clear indication that the NACA2509 foil is the one that cause the best overall turbine performance. It is notable that the differences in efficiency between the different foils is fairly constant. This implies that a further extension of the simulation cases to higher loads would yield the same results. This is of course only an implication, but the available data does certainly not imply that the NACA-2509 should suddenly perform better than the rest at a higher load. So far only performance has been taken into consideration. A major subject of this thesis has also been flow stability, vibrations and wear on the runner. Chapter 6.2 concern the variation of torque on the runner, which ultimately lead to variation in the generator output. The torque monitors show that the torque varies around a well defined mean. Obviously, by equation 6.2, the mean torque is independent of guide vane profile at any particular power output. Thus the indication in figure 6.2 is that the magnitude of torque variations might be guide vane dependent. The magnitude of variations has been more clearly illustrated in figure 6.3, and again the NACA2509 performs the best. When comparing the torque variation to figure 6.1 one see that the relative ranks between the NACA profiles are the same. There seems to be a connection between the magnitude of torque variations and turbine efficiency. This connection does not, however, explain the results. Efficiency and torque variations on the runner are merely two 'downstream' effects of how the

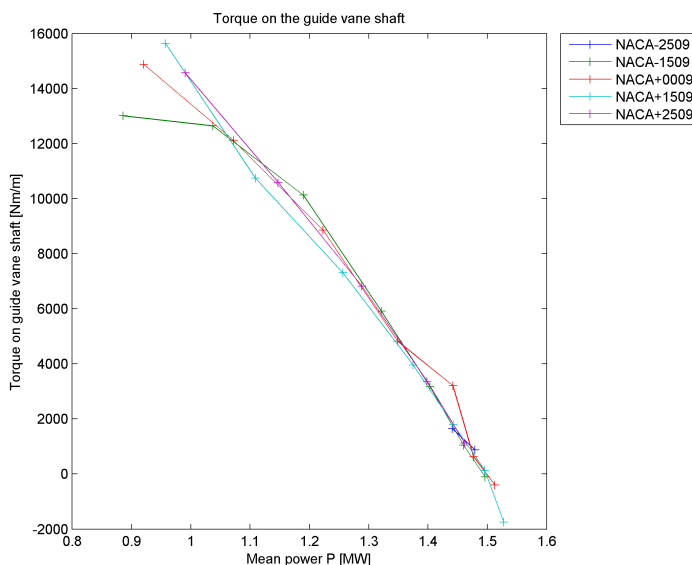


Figure 6.8: Torque on the guide vane shaft, positive direction is 'with the clock'.

guide vanes interfere with the flow. The main topic of this discussion should be the explanation of these interferences.

There are two inherently different wakes occurring behind the guide vanes, of which one; the pressure wake, is strictly not a wake but a gradient. With knowledge of the velocity diagram concept it is relatively easy to understand the effect of the velocity wake. When the runner leading edge enters the wake, the relative flow direction change. More precisely it turns towards it, creating a small relative velocity component opposing the runner rotation. Obviously this will lead to a small reduction of the runner shaft torque. The pressure gradient is caused by the flow regimes on the pressure and suction side of the guide vane. The pressure gradient across the guide vane is the cause of leak flows between the guide vane and the hub or shroud. However, the short distance means the sharp pressure gradient issue at the guide vane trailing edge is not entirely distributed when the flow reach the runner inlet. Figure 6.11 shows that the relatively even pressure distributions in the runner interior is not present at the inlet, or leading edge. Thus one might expect that there is some variation in the pressure difference between pressure and suction side on the leading edge section of the runner blade as it passes a guide vane. It seems reasonable to blame torque variations with origin in this region on these two phenomena. The effect of the guide vane on the flow is reflected in force exchange between it and the flow. Pressure interaction is commonly recognized by the lift and pressure drag, while viscous interactions are readily illustrated by the velocity wake behind the foil. By figuring out the relationship between these



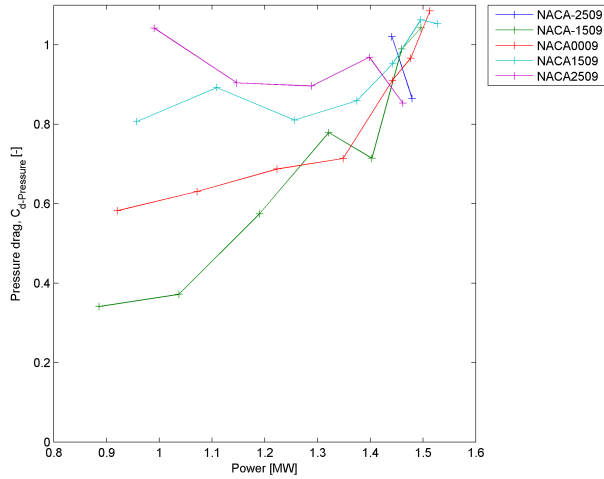


Figure 6.9: Pressure drag on the guide vane.

parameters and the observed performance and torque variations, one might be able to explain which feature is the major contributor to better performance and reduced wear.

Chapter 6.3 give account of the velocity wakes. Figures 6.4 show that the simulations consistently calculate the wakes of the NACA2509 to have the greatest width. They are however also generally on the averagely deep part of the range, that is the minimum velocity of the wake is generally not lower than for some of the other foils. It is perhaps more peculiar that at high loads the wakes are substantially wider than their counterparts. These finds are perhaps by themselves not the most informative, as they appear to be quite counterintuitive. The wider wake imply a larger viscous effect, i.e. loss, so why do increased drag cause increased efficiency? Chapter 6.4 present the force calculations based on the blade loading data. The viscous and pressure drag components are summed and graphically presented as the total drag in figure 6.12. This confirm that the drag on the NACA2509 is in fact clearly the largest for most parts of the load range. However, the foil shape dependency is a lot weaker on drag than the previously discussed parameters. This is a strong indication that the viscous wake is not the major cause of torque variation and efficiency loss. Overall, the drag appear to be a poor indicator for efficiency loss and torque fluctuations.

A look further to figure 6.10, that illustrate the lift of the foil, is also a return to apparently strong foil shape dependency. Since the positive direction of lift was directed by the global pressure and suction side of the guide vanes, positive direction is radially towards the runner shaft. Reduction of lift is obviously due to less pressure difference. So, indications are that pressure difference is an important

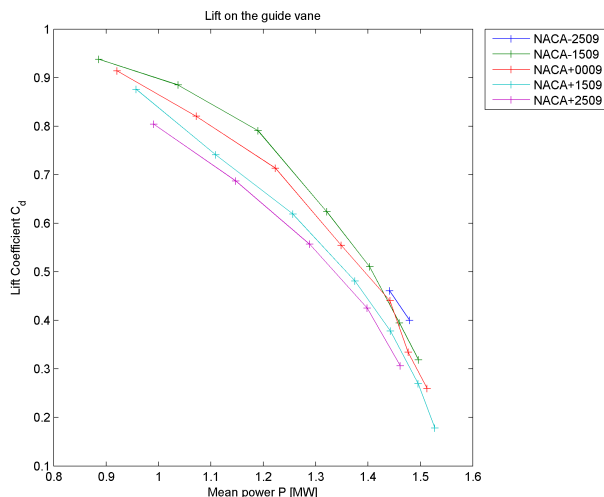


Figure 6.10: Lift on the guide vane. Positive direction towards the turbine shaft is dictated by the global pressure and suction side of the foil.

parameter in altering efficiency and torque variations. The local pressure and suction side of the NACA1509 and NACA2509 foils are opposite to the global. Thus, the flow is induced into a state of smaller pressure gradients. Judging by the simulation results, that reduce the torque fluctuation amplitude, and increase efficiency. From figure 6.13 it is apparent that velocity gradients are steeper and more restricted in space than the pressure gradients. Logically one would expect the torque fluctuation to take on a more impulse like form if velocity deficiency played a dominating role, the actual torque fluctuations are more evenly sinusoidal, see figure 6.14. Thus it would seem that all data imply the pressure gradient induced in the wicket gate is the most important contributor to torque fluctuation on the runner. The reduction of torque fluctuations are accompanied by increased efficiency.

### 6.5.1 Morphing guide vane requirements

The torque on the cambered guide vanes are not noticeably different from those of a symmetric guide vane. However, there are some additional requirements to a morphing guide vane. Some form of actuation power needs to be provided to the actual foil. As an example, let's use the 'finger concept' from Monner. The design is such that a certain arm is provided around each joint, but the joint pin will still need to carry the force on the blade. From Brekke [3] it is apparent that the maximum load on the guide vane is due to the sliding friction in addition to the hydraulic forces during opening or closing, and the total head as static pressure when the

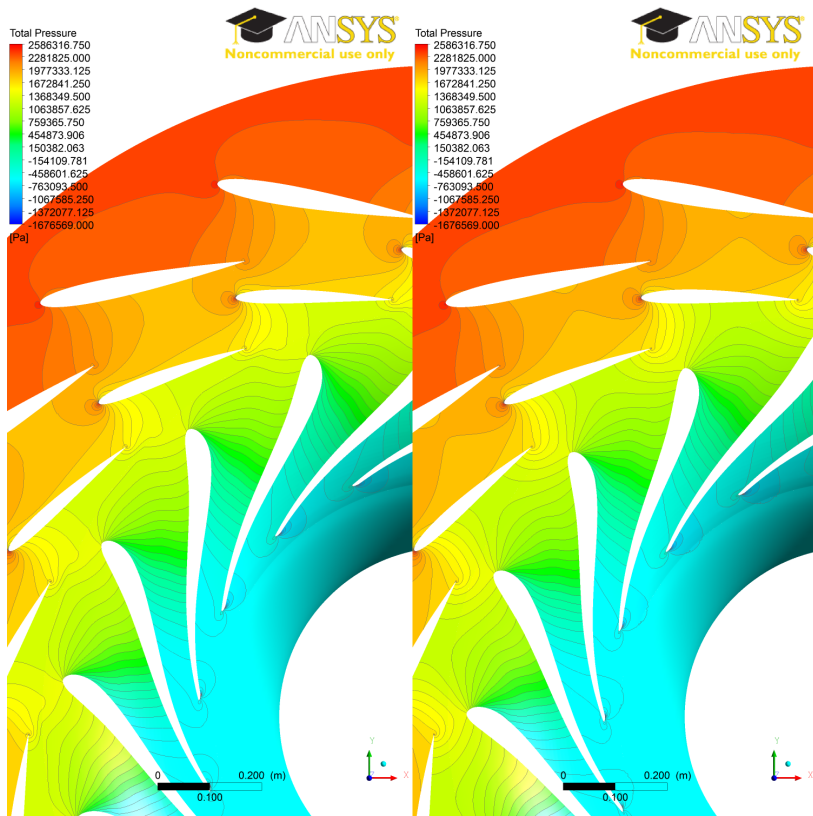


Figure 6.11: Pressure contours in the turbine, different time steps.

$\alpha$	NACAxxxx	Power [MW]	Torque [Nm/m]	$C_d$ [-]	$C_l$ [-]
16.000°	-1509	0.885	1445.921	0.343	0.938
	+0009	0.920	1653.747	0.576	0.914
	+1509	0.957	1737.678	0.783	0.876
	+2509	0.990	1618.619	0.991	0.804
18.000°	-1509	1.037	1404.927	0.364	0.885
	+0009	1.072	1346.555	0.612	0.820
	+1509	1.109	1193.422	0.859	0.741
	+2509	1.147	1176.926	0.863	0.687
20.000°	-1509	1.190	1125.385	0.563	0.791
	+0009	1.223	984.013	0.671	0.714
	+1509	1.256	812.856	0.787	0.619
	+2509	1.289	757.390	0.865	0.557
22.000°	-1509	1.321	656.672	0.763	0.624
	+0009	1.349	535.657	0.695	0.555
	+1509	1.375	439.487	0.832	0.481
	+2509	1.398	374.017	0.933	0.425
23.579°	-1509	1.403	353.549	0.694	0.510
	+0009	1.442	356.752	0.887	0.440
	+1509	1.443	199.387	0.920	0.378
	+2509	1.462	124.624	0.822	0.306
25.000°	-2509	1.441	182.840	0.990	0.461
	-1509	1.460	116.240	0.960	0.395
	+0009	1.477	70.513	0.938	0.334
	+1509	1.496	14.517	1.032	0.269
26.000°	-2509	1.479	96.841	0.841	0.400
	-1509	1.496	-12.223	1.016	0.319
	+0009	1.513	-45.102	1.060	0.260
	+1509	1.527	-194.168	1.030	0.178

Table 6.2: An overview of the guide vane force results

wicket gate is closed. It has earlier<sup>1</sup> been suggested that fluid power delivered to the foil for cambering actuation might also be used to operate inflatable seals between the blade and the wall. In that situation friction would be eliminated. This leaves the closed wicket gate as the design condition for the strength of a morphing guide vane. According to Brekke the force or torque requirement is a sealing pressure of twice the total head, which means the strength requirement of a morphing guide vane is dependent on the head of the turbine in question. This load needs to be carried by the pin joints and the construction needs to be supported by the fluid power actuator. It is apparent that most of the torque on the shaft is provided by its outermost layers, and it should be possible to provide fluid power through the center of the shaft. This leaves the pin joints as the most exposed parts, even if

---

<sup>1</sup>chapter 3.4.2

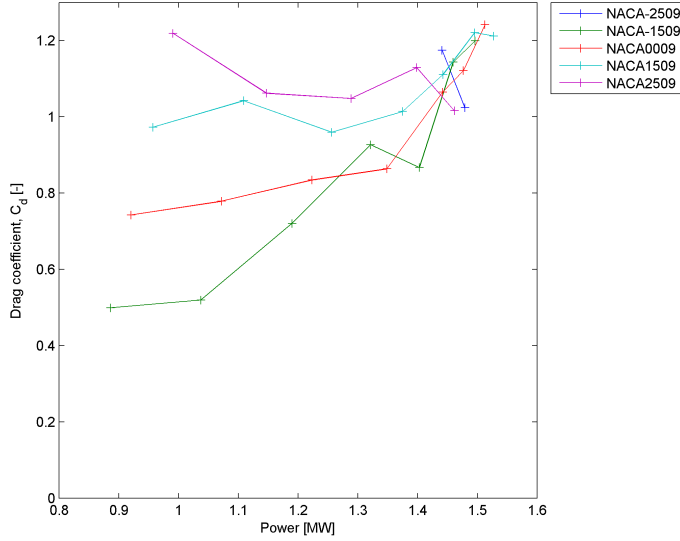


Figure 6.12: The total drag, both pressure and viscous, on a guide vane.

the assembly may be stacked to distribute load.

The author finds that all results suggest that a morphing guide vane is mechanically most feasible in low head power plants. The CFD results also suggest that the camber morphing guide vane has the biggest potential where a power plant is forced to run in a large load range. Such power plants are for instance run-of-river power plants. If increased efficiency at part loads can be achieved by camber morphing guide vanes, it might be possible to build power plants with fewer and bigger turbines, without loss of production freedom. This is of course on the premise that further investigations show that more extreme cambers can provide additional gains at part loads.

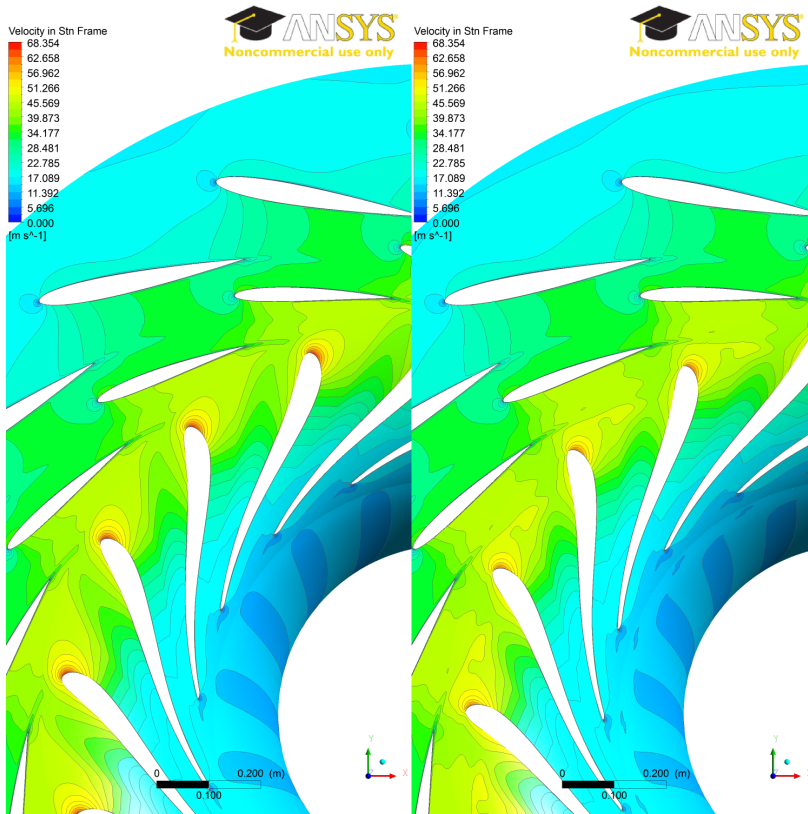


Figure 6.13: Velocity contours in the turbine, different time steps.

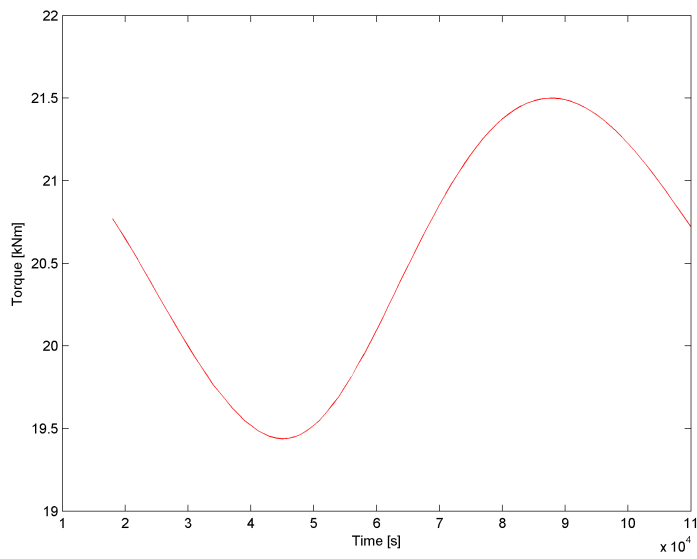


Figure 6.14: Torque fluctuation of a blade pass.





## Chapter 7

# Conclusion and further work

The CFD simulation case array was designed according to the hypothesis, according to the idea that wake size is the major parameter in determining torque fluctuation magnitude. This has been refuted by the present study. The conclusion of this study is that guide vane lift plays a large role compared to drag in the induction of torque fluctuations. At all part loads there is strong correlation between the runner torque fluctuation magnitude and pressure difference, interpreted as lift, across the different foils. The present study implies that the same mechanism does not apply to high loads, as the correlation is not present there. The cambers has been relatively modest in this study, with a maximum of 2% in each direction. It is the author's belief that larger positive cambers should be investigated at part loads. From the present results it seems that a morphing guide vane should morph from large camber at low part loads, to a moderate camber like the one seen in this study at the bestpoint. It is assumed that at some point increased drag will contribute significantly to losses, and cancel the gains from further increased lift. A more bulky - more cambered - foil might provide even larger efficiency gains at part load than seen here, while it might prove too bulky at best point load. The author's conclusion that the pressure gradient dominates the velocity wake in the induction of runner torque fluctuation is not in accordance with e.g. Antonsen [5], who does not distinguish the importance of the two.

It is the author's belief that a scientist should not become dependent of his hypothesis, but report what is actually observed. It is of course quite impossible not to develop some sort of personal hobbyhorse, but one should not let it eclipse one's results. In this thesis the results turned out to contradict the author's expectations, namely that the width and velocity deficiency of the viscous wake would dominate the torque fluctuations and that camber morphing could provide a minimum wake width for any load. This was not the result of the study. Nevertheless a parameter study on the effect of guide vane camber has been performed, and a relatively unambiguous data set is the result. If one were to dismiss data that is not in accordance with the wanted results, one might as well dismiss the project to

begin with. There is still room for the discovery of a camber morphing scheme that will improve turbine performance, and the indications of this study might prove helpful. If further studies conclude that camber morphing guide vanes can not improve turbine performance to a higher level than constant camber guide vanes, one will at the very least have good data for determining ideal camber.

# Bibliography

- [1] [http://commons.wikimedia.org/wiki/File:Francis\\_Turbine\\_High\\_flow.jpg](http://commons.wikimedia.org/wiki/File:Francis_Turbine_High_flow.jpg).
- [2] Sølvi Eide. *Numerical analysis of the head covers deflection and the leakage flow in the guide vanes of high head Francis turbines*. PhD thesis, NTNU, 2004.
- [3] Hermod Brekke. *Pumper & Turbiner*. Vannkraftlaboratoriet NTNU, 2003.
- [4] Frank M. White. *Fluid Mechanics International Edition*. McGraw-Hill, 6th edition, 2006.
- [5] Øyvind Antonsen. *Unsteady flow in wicket gate and runner with focus on static and dynamic load on runner*. PhD thesis, NTNU, 2007.
- [6] Jarle Vikør Ekanger. Ustabilitetar i sugerøyrstrømning i vasskraftturbinar - eksperimentelle studier i swirlrigg. Project Thesis, NTNU, 2010.
- [7] WJ Rheingans. Power Swings in Hydroelectric Power Plants. *Transactions of the ASME*, 1940.
- [8] Håkon Hjort Francke. *Increasing hydro turbine operation range and efficiencies using water injection in draft tubes*. PhD thesis, NTNU, 2010.
- [9] Torbjørn Nielsen and Øyvind Antonsen. Cfd simulation of von karman vortex shedding. In *22nd IAHR Symposium on Hydraulic Machinery and Systems*, 2004.
- [10] Øyvind Antonsen. Ustabile driftsområder for Francisturbiner. Project Thesis, NTNU, 2002.
- [11] B. J. Maclean and R. A. Decker. Lift analysis of a variable camber foil using the discrete vortex-blob method. *AIAA Journal*, 32(7), 1994.
- [12] A. Ya. Aronson et al. Experience in operating hydraulic structures and equipment of hydroelectric stations. *Translated from Gidrotekhnicheskoe Stroitel'stvo*, 1986.
- [13] Arpad A. Fay. Analysis of separated flows in hydro turbines, 2008.

- [14] R. M. Donaldson. Hydraulic-Turbine Runner Vibration. *Transactions of the ASME*, 1956.
- [15] Gunnar Heskestad and D. R. Olberts. Influence of Trailing-Edge Geometry on Hydraulic-Turbine-Blade Vibration Resulting from Vortex Excitation. *Journal of Engineering for Power*, 1960.
- [16] C. A. Gongwer. A Study of Vanes Singing in Water. *Journal of Applied Mechanics*, vol. 19, *Trans. ASME*, vol. 74, pp. 432-438, 1952.
- [17] Philippe Ausoni et al. Vortex shedding from blunt and oblique trailing edge hydrofoils, 2009.
- [18] Philippe Ausoni et al. Cavitation Influence on von Kármán Vortex Shedding and Induced Hydrofoil Vibrations. *Transactions of the ASME*, 129, 2007.
- [19] Theodore von Kármán. Über den mechanismus des widerstandes, den ein bewegter körper in einer flüssigkeit erzeugt. 1911.
- [20] Frank M. White. *Viscous fluid flow International Edition*. McGraw-Hill, 3rd edition, 2006.
- [21] Philippe Ausoni et al. Hydrofoil roughness effects on von kármán vortex shedding, 2007.
- [22] J. C. Owen and P. W. Bearman. Reduction of bluff-body drag and suppression of vortex shedding by the introduction of wavy separation lines. *Journal of Fluids and Structures*, 1998.
- [23] J. C. Owen and P. W. Bearman. Passive control of VIV with drag reduction. *Journal of Fluids and Structures*, 2001.
- [24] S. Szepessy and P. W. Bearman. Aspect ratio and end plate effects on vortex shedding from a circular cylinder. *J. Fluid Mech.*, 234:191–217, 1992.
- [25] Raghavan A. Kumar et al. Passive control of vortex-induced vibrations: an overview. *Recent Patents on Mechanical Engineering*, 2008.
- [26] X. Y. Huang. Feedback control of vortex shedding from a circular cylinder. *Experiments in Fluids*, 20:218–224, 1996.
- [27] R. D. Blevins. The effect of sound on vortex shedding from cylinders. *J. Fluid Mech.*, 1985.
- [28] J. E. Ffowcs Williams and B. C. Zhao. Active control of vortex shedding. *Journal of Fluids and Structures*, 1989.
- [29] Yang Liu et al. Vortex-induced vibration control by micro actuator. *Journal of Mechanical Science and Technology*, 21:1408–1414, 2007.
- [30] Chen Zhi-Hua et al. Open loop control of vortex-induced vibration of a circular cylinder. *Chinese Phys.*, 16, 2007.

- [31] A. Baz and J. Ro. Active control of flow-induced vibrations of a flexible cylinder using direct velocity feedback. *Journal of Sound and Vibration*, 1991.
- [32] Monica Sanda Iliescu. Analysis of the Cavitating Draft Tube Vortex in a Francis Turbine Using Particle Image Velocimetry Measurements in a Two-Phase Flow. *Journal of Fluids Engineering*, (130), 2008.
- [33] Romeo Susan-Resiga. Analysis of the Swirling Flow Downstream a Francis Turbine Runner. *Journal of Fluids Engineering*, (128), 2006.
- [34] Christophe Nicolet. Identification and modeling of pressure fluctuations of a Francis turbine scale model at part load operation. *22nd IAHR Symposium on Hydraulic Machinery and Systems - Stockholm*, 2004.
- [35] C. Thill et al. Morphing skins. *The Aeronautical Journal*, 2008.
- [36] Deepak S. Ramrakhyani et al. Aircraft structural morphing using tendon-actuated compliant cellular trusses. *Journal of Aircraft*, 2005.
- [37] Farhan Gandhi and Phuriwat Anusonti-Inthra. Skin design studies for variable camber morphing airfoils. *Smart Materials and Structures*, 2008.
- [38] D. Baker et al. Active truss structures for wing morphing. In *II ECCOMAS Thematic Conference on Smart Structures and Materials*, 2005.
- [39] D. Baker and Michael I. Friswell. The design of morphing aerofoils using compliant mechanisms. In *19th International Conference on Adaptive Structures and Technologies*, 2008.
- [40] D. Baker and M. I. Friswell. Determinate structures for wing camber control. *Smart Materials and Structures*, 2009.
- [41] L. F. Campanile and D. Sachau. Belt-rib concept: a structonic approach to variable camber. *Journal of Intelligent Material Systems and Structures*, 2000.
- [42] L. F. Campanile and S. Anders. Aerodynamic and aeroelastic amplification in adaptive belt-rib airfoils. *Aerospace Science and Tech*, 2005.
- [43] D. A. Perkins et al. Morphing wing structures for loitering air vehicles. *American Institute Aeronautics and Astronautics*, 2004.
- [44] D. A. Perkins et al. Adaptive wing structures. In *Smart Structures and Materials and Nondestructive Evaluation for Health Monitoring and Diagnostics conference*, 2004.
- [45] J. L. Reed et al. Adaptive wing structures. In *Smart Structures and Materials and Nondestructive Evaluation for Health Monitoring and Diagnostics conference*, 2005.
- [46] J. N. Kudva. Overview of the DARPA smart wing project. *Journal of Intelligent Material Systems and Structures*, 2004.

- [47] H. P. Monner. Design aspects of the elastic trailing edge for an adaptive wing. In *RTO MP-36*, 1999.
- [48] Michael Thomas Kikuta. Mechanical properties of candidate materials for morphing wings. Technical report, Virginia Polytechnic Institute and State University, 2003.
- [49] Larry D. Peel et al. Batch fabrication of fiber-reinforced elastomer prepreg. *Journal of Advanced Materials*, 1998.
- [50] Gabriel Murray et al. Flexible matrix composite skins for one-dimensional wing morphing. *Journal of Intelligent Material Systems and Structures*, 2010.
- [51] T. Yokozeki. Mechanical properties of corrugated composites for candidate materials of flexible wing structures. *Applied Science and Manufacturing*, 2006.
- [52] B. O. Gordon and W.W. Clark. Morphing structures by way of stiffness variations. In *48th AIAA/ASME/ASCE/AHS/ASC Structures, Structural Dynamics, and Materials Conference, Honolulu, Hawaii*, 2007.
- [53] Helge Aa. Madsen et al. The potentials of the controllable rubber trailing edge flap (CRTEF). In *EWEC 2010 Proceedings online*, page 11, 2010.
- [54] Florian R. Menter. Review of the shear-stress transport turbulence model experience from an industrial perspective. *International Journal of Computational Fluid Dynamics*, 2009.
- [55] ANSYS. TurboGrid User's Guide. [https://www1.ansys.com/customer/content/documentation/130/tg\\_user.pdf](https://www1.ansys.com/customer/content/documentation/130/tg_user.pdf).

# Appendices





# Appendix A

## Demonstration rig - Technical details

### Cylinder details

Length of active section: 440 mm

Diameter (outer): 104 mm

Hole diameter: 60 mm

Inner tube: 4 inch motorcycle tyre inner tube, checkvalve removed.

### Measurement devices

Acquisition card: National Instruments USB-6211; acquiring analog signals from the pressure transducer and vortex sensor and transmitting digital signals to the valves.

Pressure transducer: Druck PTX1400, S/N: Z00227/7, range: 4 barg

Vortex sensor: Two strain gages in a Wheatstone-bridge, amplified by a HBA DA12/MA10 (NTNU V2755-7) amplifier. Mounted on a flexible steel rod.

Velocity meter: Sensa RC2 'Duckbill', inductive type flow meter. Serial port acquisition.

### Valves

Adjustable pressure reduction valve:

Working valves: 2x *Honeywell Lucifer SA* Skinner Valve, W/N: 02 ABA 1092 A

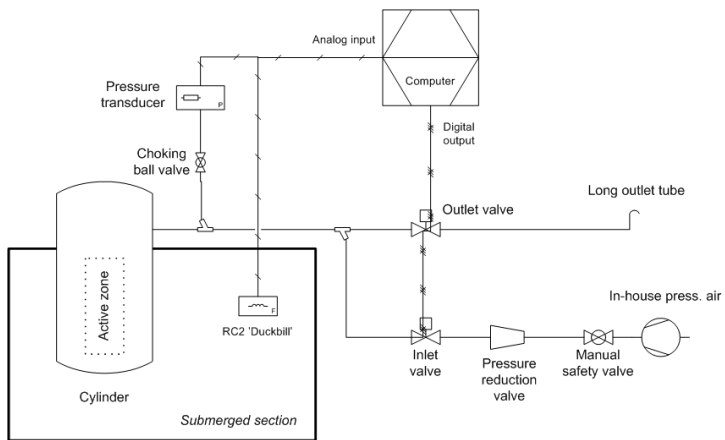


Figure A.1: Schematic of the entire rig system

## Appendix B

# Experimental work

### **B.1 First test measurements**

During this session the holes in the cylinder had a diameter of 40 mm.

### **B.2 Second test measurements**

During this session the holes in the cylinder had a diameter of 60 mm.

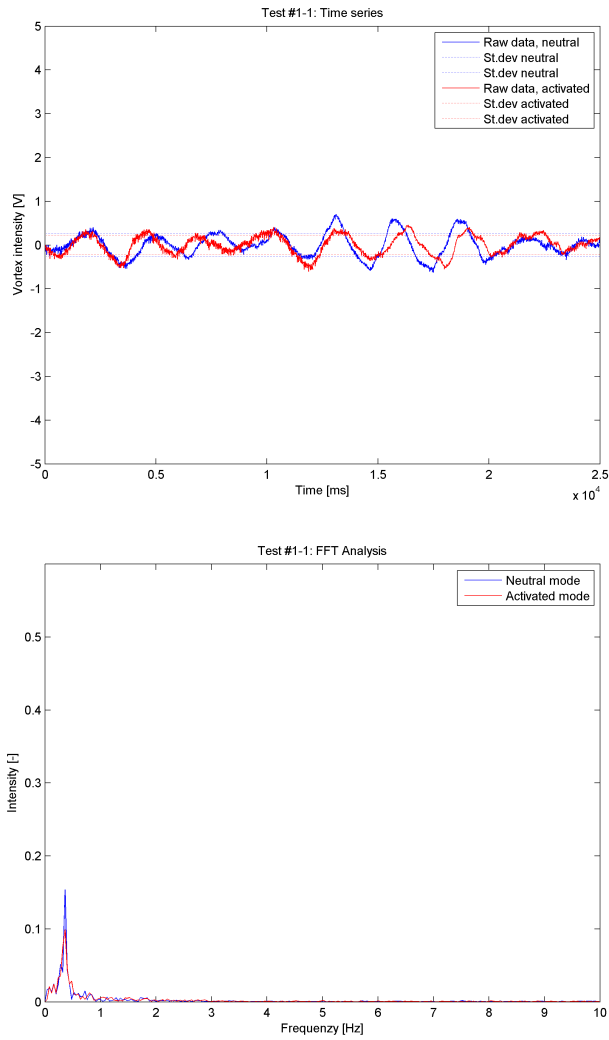


Figure B.1: Time series of the 1st run of the first measurement session.

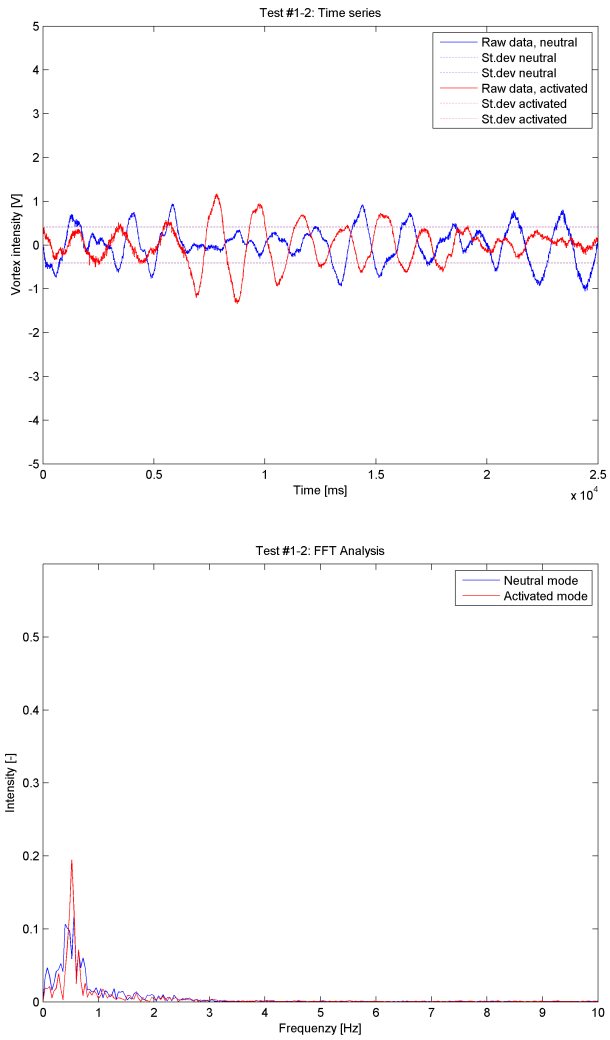


Figure B.2: Time series of the 2nd run of the first measurement session.

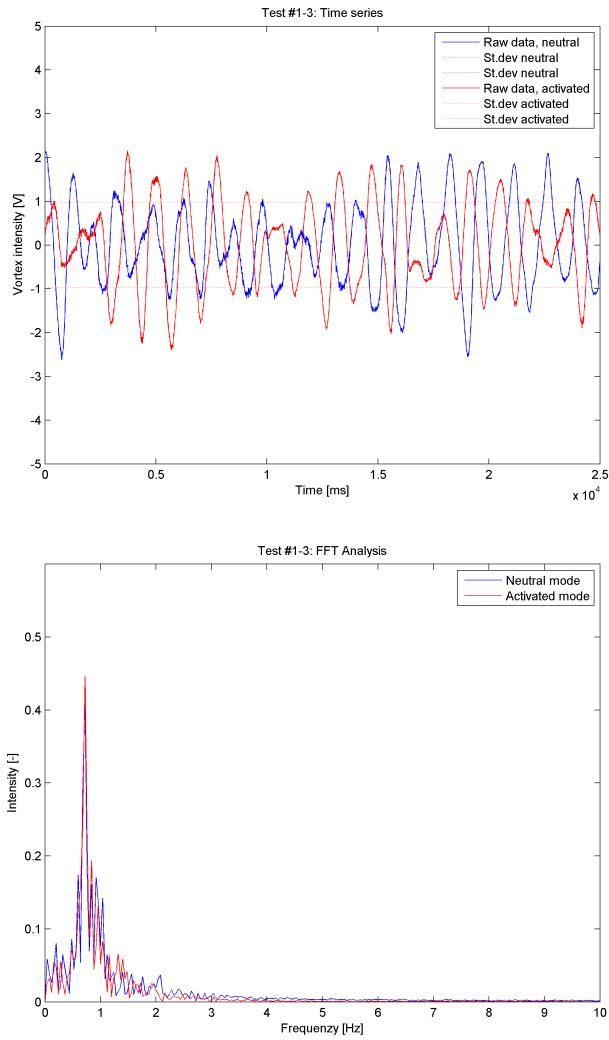


Figure B.3: Time series of the 3rd run of the first measurement session.

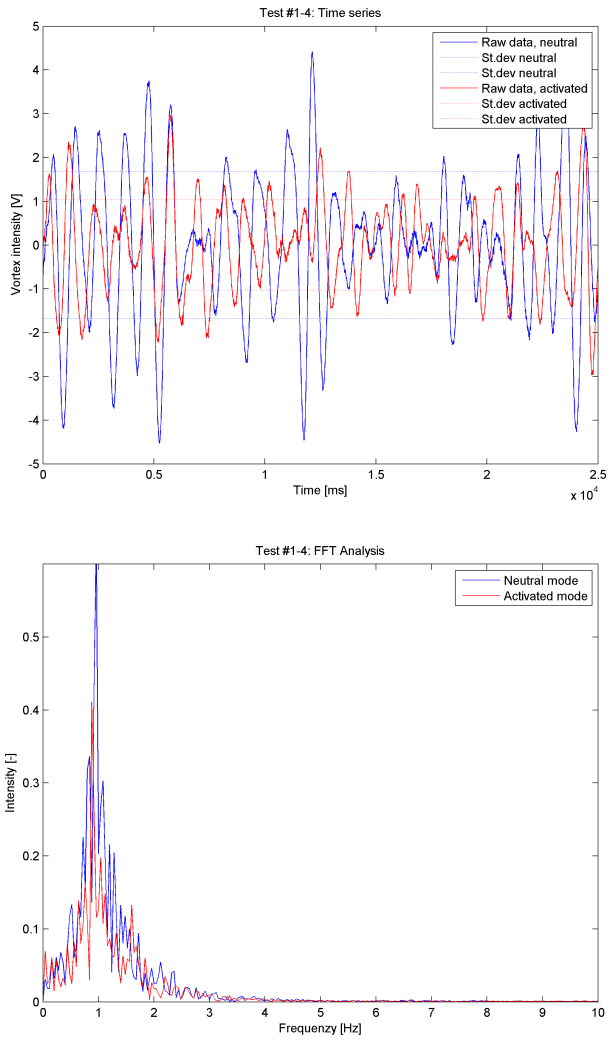


Figure B.4: Time series of the 4th run of the first measurement session.

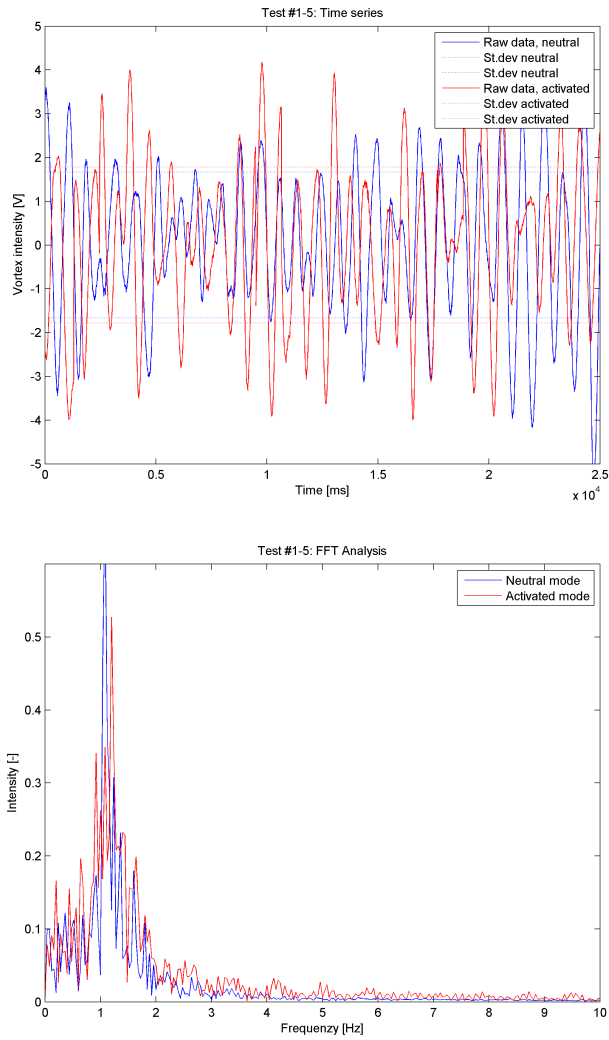


Figure B.5: Time series of the 5th run of the first measurement session.



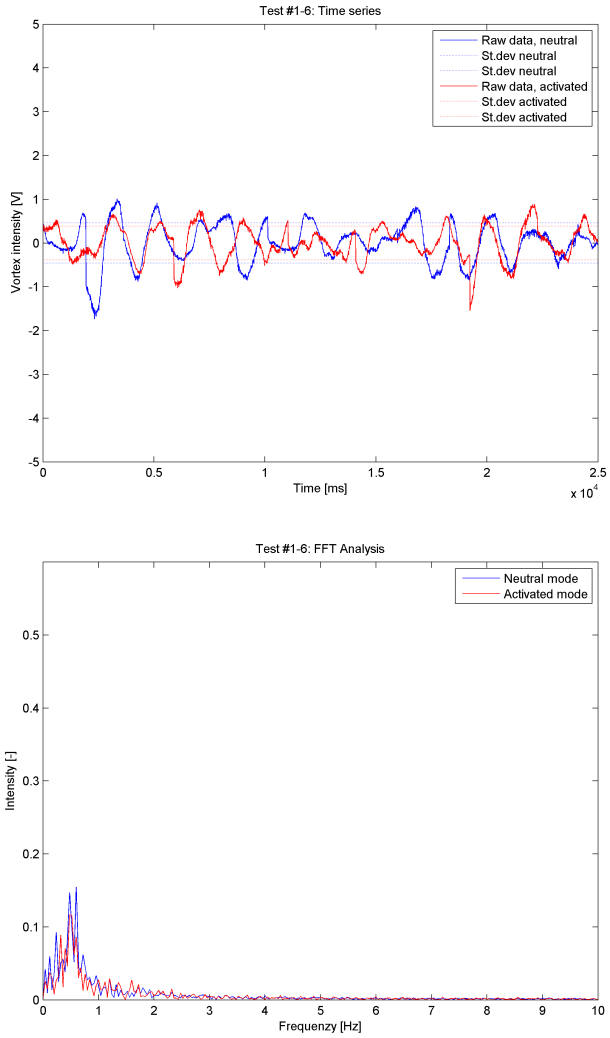


Figure B.6: Time series of the 6th run of the first measurement session.

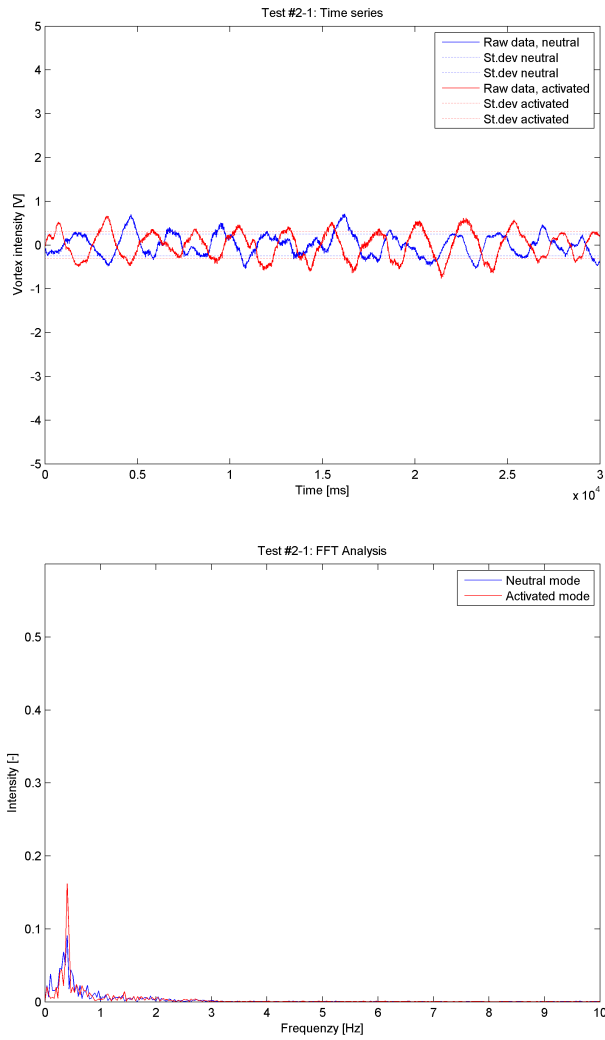


Figure B.7: Time series of the 1st run of the second measurement session.

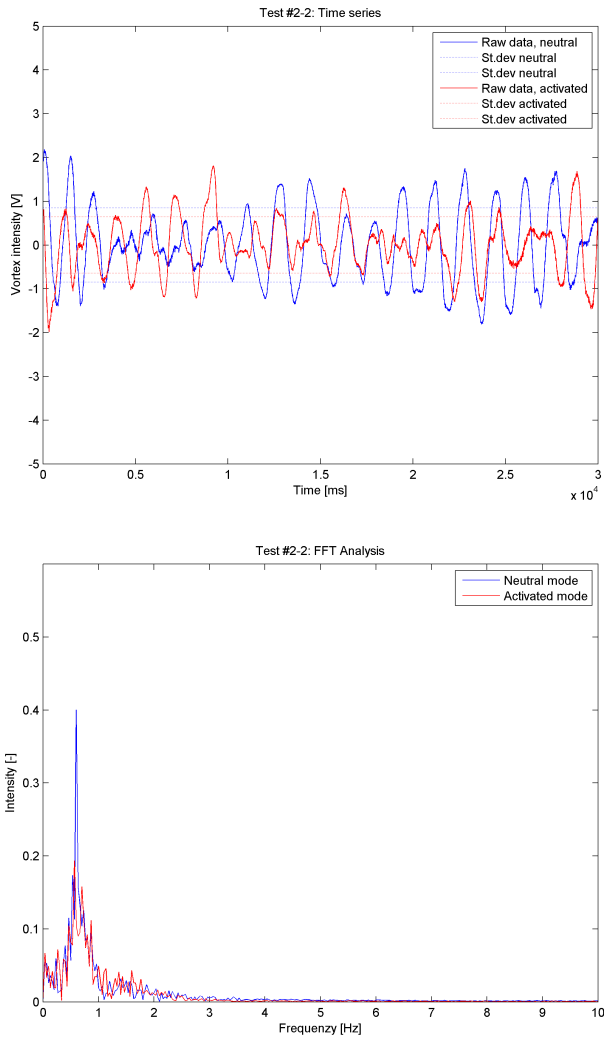


Figure B.8: Time series of the 2nd run of the second measurement session.

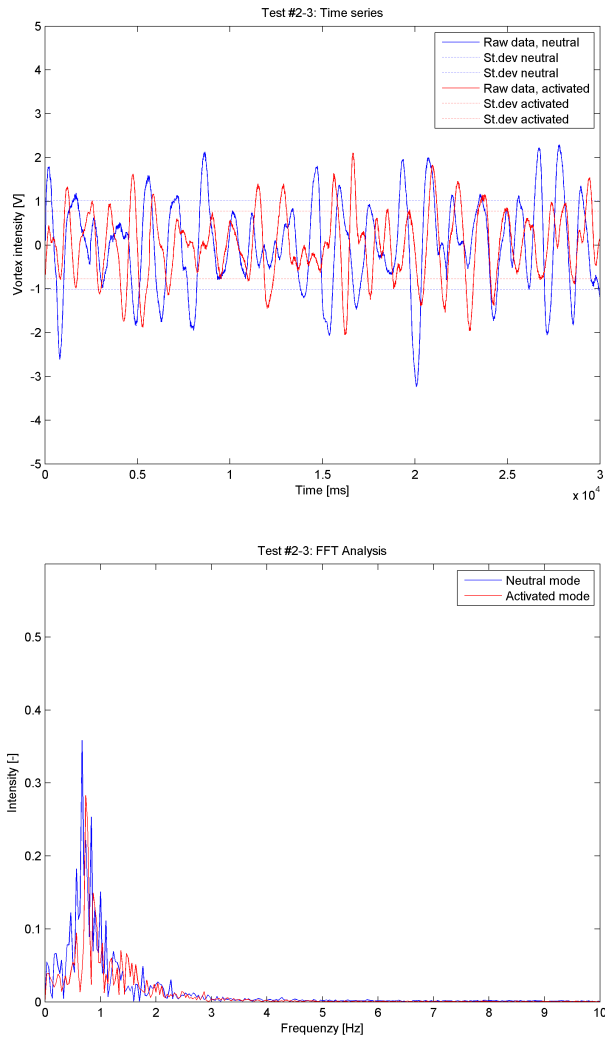


Figure B.9: Time series of the 3rd run of the second measurement session.

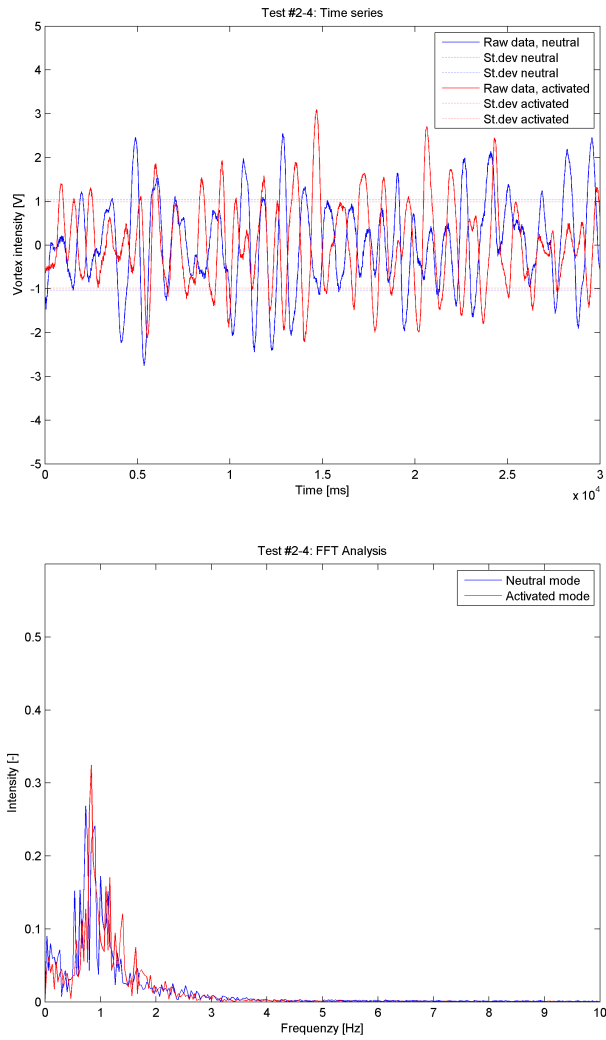


Figure B.10: Time series of the 4th run of the second measurement session.

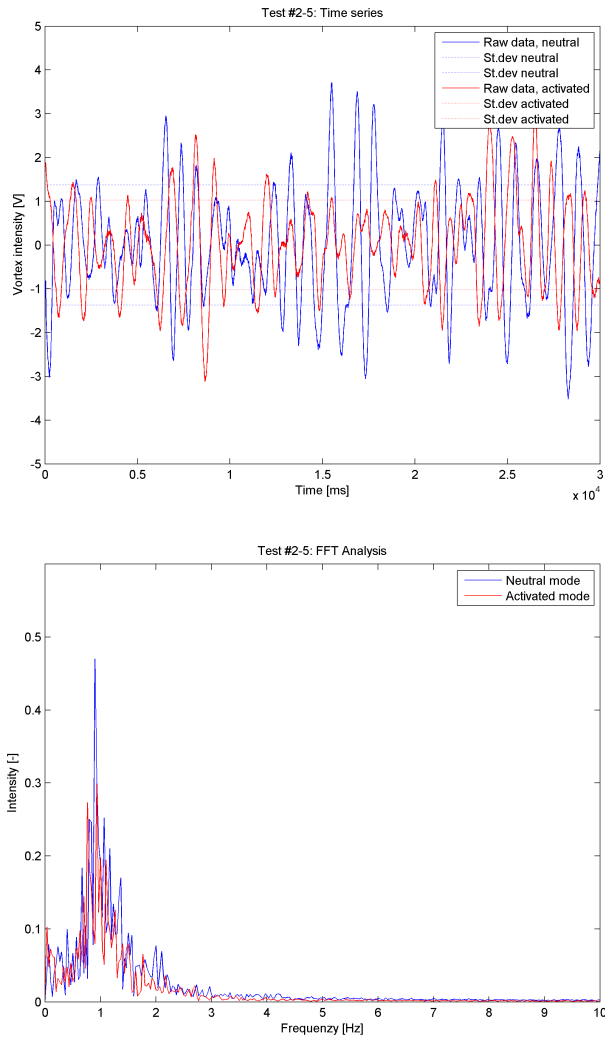


Figure B.11: Time series of the 5th run of the second measurement session.

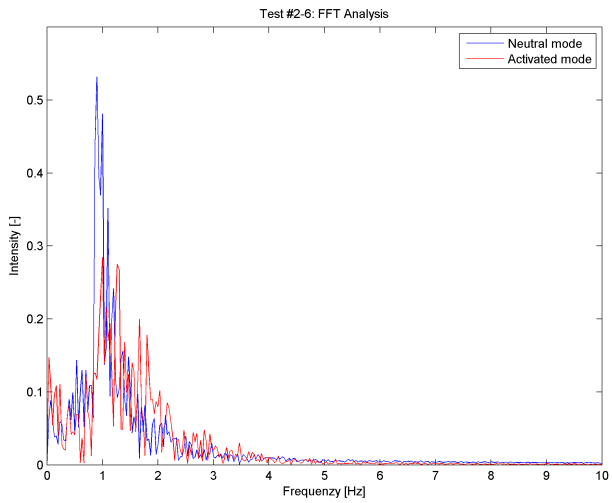
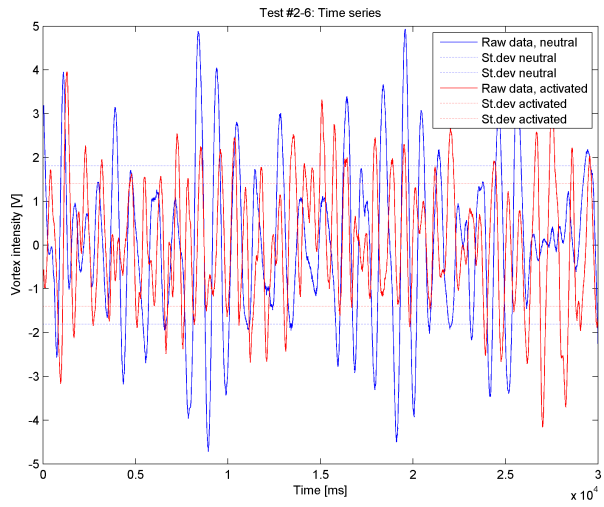


Figure B.12: Time series of the 6th run of the second measurement session.